Lithogeochemistry, Geochronology and Geodynamic Setting of the Lupa Terrane, Tanzania: Implications for the Extent of the Archean Tanzanian Craton

Christopher J.M. Lawley[a†], David Selby[a], Daniel J. Condon[b], Matthew Horstwood[b], Ian Millar[b], Quentin Crowley[c], and Jonathan Imber[a]

[a]Department of Earth Sciences, Durham University, Science Labs, Durham, DH1 3LE, UK

[b]Natural Environment Research Council Isotope Geosciences Laboratory, British Geological Survey, Keyworth, Nottingham, NG12 5GG, UK

[c]School of Natural Sciences, Department of Geology, Trinity College, Dublin 2, Ireland

[†]corresponding author email: clawley@NRCan.gc.ca; tel: (613) 996-2593

Current Address: Natural Resources Canada, Geological Survey of Canada, 601 Booth Street, Ottawa, Ontario, K1A 0E8, Canada

Abstract

Hitherto, the Lupa Terrane, SW Tanzania is a poorly understood litho-tectonic terrane comprising the Paleoproterozoic Ubendian Belt. Herein we provide new U-Pb zircon ID-TIMS, U-Pb zircon LA-MC-ICP-MS and Lu-Hf zircon LA-MC-ICP-MS results from the Lupa Terrane and demonstrate that previously considered Paleoproterozoic granitoids are in fact Archean (ca. 2.74 Ga). Foliated Archean granitoids are in turn intruded by non-foliated and voluminous Paleoproterozoic granitic–gabbroic intrusions (1.96–1.88 Ma). Archean and Paleoprotoerozic intrusive phases possess trace element characteristics that are typical of volcanic arcs and the latter possess geochemical and field evidence for crust-magma interaction. New geochemical results and field relationships suggest that the Lupa Terrane was a continental margin during the Paleoproterozoic onto which the other Ubendian litho-tectonic terranes were accreted. Our model implies at least a 150 km SW extension of the currently accepted position of the Tanzanian cratonic margin. U-Pb zircon ages constrain Ubendian tectono-magmatic models and provide new evidence to support the protracted nature of the 1.9–1.8 Ga

Ubendian accretionary history. Lu-Hf zircon model ages provide evidence for ≥3.1 Ga crust underlying the Lupa Terrane that are consistent with some of the oldest ages reported for the Tanzanian Craton and previously reported seismic tomography studies that suggest significant portions of the Ubendian Belt represent re-worked Archean lithosphere.

Keywords: Lupa Terrane, Ubendian Belt, Usagaran Belt, Tanzanian Craton, Eburnian Orogeny, Paleoproterozoic

1 Introduction

Archean cratonic margins are complex geologic settings characterized by overprinting structural, magmatic, and metamorphic events (e.g., Zhoa et al., 2002; Reddy and Evans, 2009). This is particularly apparent in the Paleoproterozoic Ubendian and Usagaran metamorphic Belts which border the western and southern margins of the Tanzania Craton, respectively. Existing models for the Paleoproterozoic tectonic evolution of the Tanzanian cratonic margin invoke thrust-dominated accretion of terranes comprising the Usagaran Belt coupled with lateral accretion of terranes comprising the Ubendian Belt (Daly, 1988; Lenoir et al., 1994). However, recent geochronologic evidence suggests that the current configuration of the Ubendian Terranes is the product of at least three discrete orogenic events that are correlated to the Ubendian, Kibaran and Pan-African orogenic episodes (Boniface et al., 2012; Boniface and Schenk, 2012). The Paleoproterozoic tectonic history of the Ubendian Belt and the Tanzanian cratonic margin therefore remains poorly understood due, in part, to Neoproterozoic and Pan-African cover rocks, Meso- and Neoproterozoic metamorphic overprints, and periodic reactivation of geologic structures from the Paleoproterozoic until the present day (Theunissen et al., 1996).

The Lupa Terrane is located adjacent to the Tanzanian Craton and is the least-understood of the eight litho-tectonic terranes comprising the Ubendian Belt (Figs. 1–2; Daly, 1988). Voluminous granitoids intruding the Lupa Terrane that obscure the southern extent of the Tanzanian cratonic margin have, hitherto been attributed to widespread Paleoproterozoic magmatic activity related to the Ubendian Orogeny (e.g., Sommer et al., 2005). Herein we characterize and date these and other major

lithologies in the Lupa Terrane and place constraints on the Paleoproterozoic geodynamic evolution of the Ubendian Belt. New U-Pb zircon LA-MC-ICP-MS ages, coupled with Lu-Hf zircon LA-MC-ICP-MS results, call into question the currently accepted SW extent of the Tanzanian cratonic margin (Manya, 2011). Establishing the extent of the Tanzanian Craton places important constraints on the prospectivity of SW Tanzania for ore deposits associated with Archean Cratons (e.g., orogenic Au deposits; Sango, 1988; Lawley, 2012).

2 Geologic Setting

2.1 Regional Geology

The western margin of the Tanzanian Craton is separated from the Congo Craton and the Bangweulu Block by the ca. 600 km long and 150 km wide zone of granulite-amphibolite facies meta-igneous and meta-sedimentary rocks known as the Ubendian Belt (McConnell, 1950; Sutton et al., 1954; Lenoir et al., 1994). Current tectonic models divide the Ubendian Belt into eight lithologicaly- and structurally-defined terranes: Ubende, Wakole, Katuma, Ufipa, Mbozi, Lupa, Upangwa, and Nyika (Fig. 1a; Daly, 1988). Mesoproterozoic meta-sedimentary rocks, corresponding to the Muva Supergroup, unconformably overlie the Ubendian Belt and have been subsequently metamorphosed during the Kibaran Orogeny (Cahen et al., 1984). These rocks are in turn overlain by Neoproterozoic clastic sedimentary rocks which correspond to the Bukoban Supergroup (Cahen et al., 1984). Meso- and Neoproterozoic cover sequences blanket large areas of the Ubendian basement and obscure its northern and southern limits (Hanson, 2003).

The Ubendian Belt formed through a series of metamorphic and tectonic events that span ca. 300 Myr (Lenoir et al., 1994). The first tectonic event is constrained by U-Pb zircon and Rb-Sr whole rock dating of syntectonic magmatic intrusions at 2093–2048 Ma (Dodson et al., 1975; Lenoir et al., 1994; Ring et al., 1997). The 2.1–2.0 Ga Ubendian tectonic phase corresponds with a period of eclogite and granulite facies metamorphism, the development of a ductile E-W trending tectonic fabric and is concomitant with metamorphism in the adjacent Usagaran Belt (Lenoir et al., 1994; Collins et al., 2004). Eclogitic rocks with MORB-like chemistry from the Usagaran, dated at ca. 2.0 Ga, suggest that metamorphism and tectonism resulted from subduction zone processes analogous to

85 modern-day accretionary margins and may have resulted from the collision between the Tanzanian
86 and Congo Cratons and the Bangweulu Block (Möller et al., 1995). Structural evidence associated
87 with the 2.1–2.0 Ga Ubendian tectonic phase has largely been overprinted by later deformation, with
88 the exception of the Mbozi Terrane (Theunissen et al., 1996).

89 The 2.1–2.0 Ga Ubendian tectonic phase is overprinted by a 1.9–1.8 Ga tectonic phase that
90 produced the characteristic Terrane-bounding NW-SE trending shear zones and amphibolite facies
91 metamorphism (Lenoir et al., 1994). The exact timing of this deformation event is poorly constrained
92 and is thought to have occurred at 1860 ± 23 Ma based on a weighted average age of U-Pb and whole
93 rock Rb-Sr ages of late-kinematic granitoids (Lenoir et al., 1994; Fig. 2). This age overlaps within
94 analytical uncertainty with a weighted average Ar-Ar barroisite cooling age of 1848 ± 6 Ma from a
95 mafic tectonite that is also interpreted to record the 1.9–1.8 Ga Ubendian tectonic phase (Boven et al.,
96 1999), whereas the Kate Granite post-dates the second Ubendian tectonic phase and provides a
97 possible maximum age for deformation at ca. 1825 Ma (Rb-Sr whole rock; Schandelmeier, 1983).
98 These Rb-Sr and Ar-Ar ages are younger than recent U-Pb (SIMS) zircon dating of eclogites with
99 MORB-like chemistry that suggest high-pressure and low-temperature metamorphism, analogous to
100 modern-day subduction zones, occurred within the Ubende Terrane at 1886 ± 16 and 1866 ± 14 Ma
101 (Boniface et al., 2012). Paleoproterozoic granites and tectonites are in turn overprinted during the
102 Meso- and Neoproterozoic orogenic episodes (Theunissen et al., 1992; Ring et al., 1993; Ring et al.,
103 1997; Theunissen et al., 1996). In particular, Paleo- and Neoproterozoic-aged eclogites with MORB-
104 like chemistry represent paleo-sutures and suggest the current configuration of Ubendian Terranes is
105 the result of at least three discrete orogenic cycles (Boniface, 2009; Boniface and Schenk, 2012). Our
106 U-Pb ages place new geochronologic constraints on the timing of metamorphism, tectonism, and
107 magmatism in the Lupa Terrane and provide new evidence to support the Ubendian Belt's protracted
108 Paleoproterozoic tectonic evolution.

109 *2.2 Local Geology*

110 The geology of the Lupa Terrane has been variably described as comprising high-grade
111 gneissic, high-grade schistose rocks, and granitic gneisses (e.g., Grantham, 1931, 1932, 1933; Teale et
112 al., 1935; Gallagher, 1939; Harris, 1961; Van Straaten, 1984; Daly, 1988; Sango, 1988; Lenoir et al.,

1994). The extent of the Lupa Terrane is also unclear from the literature (e.g., Kimambo, 1984; Daly, 1988). For the purposes of this study the Lupa Terrane is assumed to be coincident with the extent of the Lupa goldfield which is defined as the triangular shaped block bounded by the Rukwa Rift Escarpment (or Lupa Border Fault; Kilembe and Rosendahl, 1992) to the west, the Mkondo Magnetic Lineament to the north (Marobhe, 1989), and the Usangu Escarpment to the east. The Rukwa and Usangu Escarpments represent Tertiary faults that are related to the East African Rift, whereas the nature of the Mkondo Magnetic Lineament is more cryptic (Marobhe, 1989). The field area for the current study is located in the northern portion of the Lupa Terrane and corresponds with the mineral exploration licenses currently controlled by Helio Resource Corp. (Fig. 3). These mineral exploration licenses contain a number of orogenic gold systems and include the Kenge and Porcupine exploration targets (e.g., Lawley, 2012; Lawley et al., in press).

Hitherto geochronology of the Lupa Terrane has been limited to a K-Ar ages from a greisen and granite at 1802 ± 70 Ma and 1827 ± 70 (Cahen et al., 1984), respectively, and two poorly constrained U-Pb zircon ages of the Ilunga Granite (1931 ± 44 Ma; MSWD = 110; n = 4) and Saza Granite (1936 ± 47 Ma; MSWD = 230; n = 4; Mnali, 1999). Two SIMS U-Pb zircon ages of the Saza granite and a cross cutting mafic dike were also dated at 1924 ± 13 (MSWD = 2.6) and 1758 ± 33 Ma (MSWD = 0.9), receptively (Manya, 2012). The Ilunga and Saza granites intruded into what has been previously mapped as a "highly-deformed acid schist" (e.g., Kimambo, 1984) and "gneiss" (e.g., Grantham, 1932; Teale, 1935; van Straaten, 1984). We provide new geologic, geochemical evidence and geochronologic evidence to re-classify these rocks and propose a geodynamic setting to explain their occurrence.

3 Analytical Methods

3.1 U-Pb Zircon ID-TIMS

The detailed analytical methodology is presented in an electronic supplement, but is briefly summarized here. All of the analyzed zircon crystals have undergone the "chemical abrasion" (thermal annealing and subsequent leaching) pre-treatment technique (Mattinson, 2005) for the

effective elimination of Pb-loss. Isotope ratios were measured at the NERC Isotope Geosciences Laboratory (NIGL), UK, using a Thermo-Electron Triton Thermal Ionisation Mass-Spectrometer (TIMS). Pb isotopes were measured by peak-hopping on a single SEM detector. U isotopic measurements were made in static Faraday mode. Age calculations and uncertainty estimation were based upon the algorithms of Schmitz and Schoene (2007).

3.2 U-Pb Zircon LA-MC-ICP-MS

This analytical methodology is also presented in detail in the electronic supplement but is briefly described here. Laser Ablation Multi-Collector Inductively Coupled Mass Spectrometry (LA-MC-ICP-MS) was completed at the NERC Isotope Geoscience Laboratory (NIGL). Zircon mineral separates were mounted in epoxy, polished, and imaged using cathodluminesence (CL) on a scanning electron microscope (SEM) at the British Geological Survey (BGS; except for CL098 which was prepared at the School of Natural Sciences, Trinity College Dublin). Zircon crystals were ablated using a New Wave Research Nd:YAG laser ablation system and isotopes ratios measured using a Nu Plasma MC-ICP-MS equipped with a multi-ion-counting array. The internationally recognized 91500 zircon standard (Weidenbeck et al., 1995) was used as the primary standard, whereas Plešovice (Sláma et al., 2008) and GJ-1 (Jackson et al., 2004) were used as secondary standards. All $^{206}Pb/^{238}U$ dates (ID-TIMS and LA-MC-ICP-MS) are calculated using the ^{238}U and ^{235}U decay constants of Jaffey et al. (Jaffey et al., 1971). The consensus value of $^{238}U/^{235}U = 137.818 \pm 0.045$ (Hiess et al., 2012) was used in the data reduction calculations for ID-TIMS and LA-MC-ICP-MS dates. Using this more accurate value with its associated uncertainty estimate has the effect of lowering $^{207}Pb/^{206}Pb$ dates at ca. 2 Ga by 0.8 ± 0.6 Myr, compared to $^{207}Pb/^{206}Pb$ dates calculated using the consensus value of $^{238}U/^{235}U = 137.88$.

3.3 Lu-Hf Zircon LA-MC-ICP-MS

Near concordant (>95% concordance) U-Pb zircon ablation sites from samples CL098, CL109, and CL1020 were re-analyzed to measure their respective Lu-Hf isotopic compositions. Isotope analyses were carried out at the NIGL using a Thermo Scientific Neptune Plus MC-ICP-MS coupled to a New Wave Research UP193FX excimer laser ablation system and low-volume ablation cell. Helium was used as the carrier gas through the ablation cell with Ar make-up gas being

connected via a T-piece and sourced from a Cetac Aridus II desolvating nebulizer. After initial set-up and tuning a 2% HNO_3 solution was aspirated during the ablation analyses. Lutetium (^{175}Lu), ytterbium (^{172}Yb, ^{173}Yb), and hafnium (^{177}Hf, ^{178}Hf, ^{179}Hf, and ^{180}Hf) isotopes were measured simultaneously during static 30s ablation analyses (50 μm; fluence = 8–10 J/cm^2). A standard–sample–standard bracketing technique, using reference zircon 91500, was used to monitor accuracy of internally corrected Hf isotope ratios and instrumental drift with respect to the Lu/Hf ratio. Hf reference solution JMC475 was analyzed during the analytical session to allow normalisation of the laser ablation Hf isotope data. Correction for ^{176}Yb on the ^{176}Hf peak was made using reverse-mass-bias correction of the $^{176}Yb/^{173}Yb$ ratio (0.7941) empirically derived using Hf mass bias corrected Yb-doped JMC475 solutions (cf. Nowell & Parrish, 2001). ^{176}Lu interference on the ^{176}Hf peak was corrected by using the measured ^{175}Lu and assuming $^{176}Lu/^{175}Lu = 0.02653$.

3.4 Lithogeochemistry

A representative suite (23 samples) of magmatic phases were analyzed for major and trace elements using a combination of fusion inductively coupled plasma-mass spectrometry (ICP-MS) and instrumental neutron activation analysis (INAA) by Actlabs (Ancaster, Ontario; method 4E-Research). Sample aliquants for ICP-MS analysis were first mixed with a lithium metaborate-tetraborate flux and fused in order to ensure complete digestion of refractory minerals (e.g., zircon). As a result, fusion ICP-MS results are considered most representative and are used for plotting purposes. Detection limits for this assay package are in the low ppm and ppb range for most trace elements. Standards, duplicates and blanks were used as a means of quality control and the difference between duplicate analyses were generally within a few ppm for most trace elements.

4 Results and Data Interpretation

4.1 Lithologies

All rocks within the field area have undergone hydrothermal alteration and greenschist facies metamorphism. Thus, all rock names are metamorphic and for the remaining discussion all rock names should have the prefix “meta-” (Figs. 4–6). Non-foliated felsic-mafic magmatic rocks intrude

into a pervasively deformed granitic unit (Figs. 4a, b, and c). Rocks lacking this pervasive tectonic fabric have been classified according to the IUGS classification scheme (LeMaitre, 2002). Two granitoids, the Saza Granodiorite and Ilunga Syenogranite (named after their outcrop localities adjacent to the town of Saza and the Ilunga Hills, respectively), are exceptions and their IUGS names are accompanied by the prefix Saza and Ilunga, respectively as a result of their regional significance (Fig. 3). Intermediate and mafic rocks are difficult to classify using the IUGS scheme because the primary mineralogy has been partially to completely replaced by amphibole (± relict pyroxene) and plagioclase (Fig. 6c). The large range of amphibole content (modes 15–60%) coupled with the large range of SiO_2 (50–60% SiO_2; see below) and Mg# (44–73; see below) suggests these rocks represent a compositional spectrum of protoliths (discussed further below). As a result, amphibole-plagioclase rocks are termed the diorite-gabbro suite in the following lithogeochemistry discussion (Mnali, 2002). Sample locations, descriptions, and modal mineralogy are presented in Table 1.

Foliated granitoids crop out in the southern portion of the field area (Fig. 3). K feldspar, quartz and plagioclase are the dominant mineral assemblage with lesser amounts of chlorite ± calcite ± titanite ± epidote. However, foliated granitoids exhibit a wide range of modal mineralogy (e.g., the modal mineralogy of foliated granitoids ranges from syenogranite to monzogranite) and likely represent several different lithologies, but have been grouped based on a distinct deformation fabric that is absent in the other identified granitoids. This characteristic foliation is defined by alternating quartz-feldspar and chlorite rich bands, which gives the rock a banded to "gneissic" appearance (Fig. 4b). Compositional banding is accompanied by crystal plastic deformation of quartz (Lawley et al., in press) and both characteristics are dissimilar to the mineralogy and deformation processes that are typical of gneissic rocks comprising the other Ubendian Terranes (Lenoir et al., 1994). Non-foliated granitoids, dioritic-gabbroic intrusions/dikes and aplitic dikes are all observed cross cutting foliated granitoids and suggest that fabric development occurred prior to widespread magmatism in the field area (Fig. 4c; Lawley et al., in press).

The Ilunga Syenogranite represents the dominant lithology in the northern portion of the field area and corresponds with a topographic high referred to as the Ilunga Hills (Fig. 3). K feldspar,

quartz and plagioclase comprise the primary mineral assemblage with lesser amounts of chloritized biotite (typically less than 10% modal abundance). The Ilunga Syenogranite is typically equigranular and coarse grained, but locally grades into finer grained and more K feldspar rich zones with aplitic texture. The finer grain size and change in modal mineralogy is also accompanied with quartz-feldspar intergrowths in thin section (Fig. 6f). K feldspar-plagioclase intergrowths are also locally observed in thin section and are unique to the Ilunga Syenogranite within the field area. Very few igneous contacts between the Ilunga Syenogranite and other lithologies were observed aside from cross cutting diorite-gabbroic intrusions at the top of the Ilunga Hills, which coupled with mafic enclaves suggests diorite-gabbroic intrusions/dikes pre- and post-date the Ilunga Syenogranite.

The regionally significant Saza Granodiorite crops out in the southern portion of the field area as a coarse grained and equigranular intrusion (Fig. 3). Quartz, plagioclase and K feldspar comprise the dominant mineral assemblage with lesser amounts of chloritized biotite and hornblende (Fe-Mg minerals generally constitute less than 5% modal abundance). Sericite, calcite and epidote are also observed overprinting the primary mineral assemblage. Abundant diorite-gabbroic enclaves/xenoliths, coupled with cross cutting dioritic-gabbroic dikes/intrusions, suggests that the Saza Granodiorite was pre- and post-dated by dioritic-gabbroic magmatism (Fig. 5e). The Saza Granodiorite is also cross cut by auriferous mylonitic shear zones and aplite dikes (Fig. 3).

Dioritic-gabbroic dikes and intrusions represent a significant proportion of the rocks exposed in the field area and are typically observed cross cutting and intruding granitoids (Fig. 3). Amphibole and plagioclase are the dominant minerals, whereas chlorite, epidote, titanite and calcite are typically present as accessory phases (Fig. 6c). Rare relict pyroxene crystals are also observed and are variably altered by a chlorite ± epidote ± titanite ± calcite alteration assemblage. The presence of diorite-gabbroic enclaves/xenoliths in all of the identified and temporally distinct granitoids (discussed further below) is consistent with multiple dioritic-gabbroic intrusive events.

A variety of other granitoids, ranging from syenogranite to tonalite in modal mineralogy, were also observed in the field area and occur as dikes and small intrusions (Fig. 3). These additional non-foliated magmatic phases are observed cross cutting foliated granitoids, but are in turn cross cut

by auriferous shear zones. Several of these magmatic phases remain undated (e.g., syenogranite; Fig. 3), however we expect that the majority of igneous activity occurred prior to mylonitization that is constrained by Re-Os sulphide ages at 1.88 Ga (Lawley et al., in press).

4.2 U-Pb Zircon ID-TIMS Results

For the detailed U-Pb zircon results see the Online Supplementary Table S1 and Fig. 7. Our interpreted crystallization ages are reported in Table 2 and were calculated using Isoplot v. 4.15 (Ludwig, 2008). The preferred crystallization age for each of the three samples is a weighted average $^{207}Pb/^{206}Pb$ age of concordant analyses because these zircon crystals exhibit the least evidence of disturbance and are the most likely to record crystallization ages. Sample CL0972 is a zircon mineral separate from the Ilunga Syenogranite that hosts the Porcupine ore body. Concordant zircon crystals from CL0972 yield a weighted average $^{207}Pb/^{206}Pb$ age of 1959.6 ± 1.0 (MSWD = 1.4; n = 5). Sample CL0975 is a zircon mineral separate from the Saza Granodiorite. Concordant zircon crystals from this sample yield a weighted average $^{207}Pb/^{206}Pb$ age of 1934.5 ± 1.0 (MSWD = 1.7; n = 5). Sample CL0911 is a zircon mineral separate from a non-foliated granodiorite dike that is observed cross cutting the foliated granitoid at the Kenge ore body (CL098 dated by LA-MC-ICP-MS; Fig. 4c). Concordant zircon crystals from sample CL0911 yield a weighted average $^{207}Pb/^{206}Pb$ age of 1958.5 ± 1.3 (MSWD = 0.41; n = 2), consistent with the less precise upper intercept date of 1964.6 ± 5.4 (MSWD = 3.6; n = 5). The lower intercept age of 1126 ± 150 Ma (MSWD = 3.6; n = 5) could represent a Pb-loss event during the Mesoproterozoic that is consistent with the timing of the Kibaran Orogeny (Boniface et al., 2012). In addition to determining the crystallization age of CL0911, U-Pb ages also constrain the maximum age of deformation for CL098 (see section 4.5).

4.3 U-Pb Zircon LA-MC-ICP-MS Results

All Cathodoluminesence (CL) images and ablation spot locations are provided as Online Supplementary Figures (see Online Supplementary Figs. S1–S6). Reference material analyses and sample results are provided as Online Supplementary Tables (see Online Supplementary Tables S2–S7). Data are presented on Concordia plots in Figures 9 and 10. Our preferred crystallization ages are reported in Table 2 and were calculated using Isoplot v. 4.15 (Ludwig, 2008). All zircon grains

277 possess euhedral crystal shapes and complex magmatic oscillatory zoning characterized by truncated
278 and resorbed growth phases. Zircon recrystallization is also suspected in weakly luminescent zircon
279 zones that lack oscillatory zoning (Fig. 8).

280 Sample CL098 is a foliated granitoid that hosts the Kenge Au ore body. Twenty-six ablation
281 analyses were measured from seventeen zircon crystals. Two of these analyses (zircon crystals 12-1
282 and 18-2) possessed significant common lead (1.7–3.8% f^{206}Pbc) and are therefore not shown in Figs.
283 9a, b. We consider the fifteen concordant (100 ± 2% concordance) analyses to reflect the best
284 determination of the actual crystallization age of the sample and yield a weighted average ^{207}Pb/^{206}Pb
285 age of 2723 ± 10 Ma (± 40 2 SD; MSWD = 5.8; n = 17). The large MSWD implies the assigned
286 analytical uncertainties do not account for the observed U-Pb age range. Therefore, our dataset likely
287 contains multiple zircon populations that possess similar but distinct ages that partially overlap within
288 analytical uncertainty of individual analyses.

289 Sample CL109 is a foliated granitoid with a well-developed S- and L-fabric. Thirty-seven
290 ablation spots from seventeen zircon crystals were analyzed. The majority of imaged zircon crystals
291 from CL109 possess a bright and very-narrow rim that was not possible to analyse with a 25 μm spot
292 size (Fig. 9a). Three of these zircon crystals (zircon crystals C5-1, C6-1, and H1-2) possess
293 significant common lead (1.5–1.8% f^{206}Pbc) and are not shown in Figs. 9a, b. The remaining zircon
294 crystals constrain a Model-2 York fit regression with an upper intercept age of 2754 ±14 Ma and
295 lower intercept age at 512 ± 140 Ma (MSWD = 16; n = 34). The large MSWD reflects considerable
296 scatter along the discordia curve and is indicative of complex and non-zero Pb-loss. The youngest
297 ^{207}Pb/^{206}Pb ages correspond to what appear from CL images to be recrystallized zircon crystals;
298 however several of the younger ^{207}Pb/^{206}Pb ages correspond with magmatically zoned and pristine
299 portions of the zircon crystals. One of these analyses (J2-1) overlaps multiple growth zones,
300 corresponds to a brightly-luminescent margin of the zircon, and possesses an anomalously low
301 ^{207}Pb/^{206}Pb age at 2620 ± 17 Ma. If this analysis is excluded, a weighted average ^{207}Pb/^{206}Pb age for
302 the remaining most concordant zircon crystals (>98% concordance) is 2758 ± 9 Ma (± 28 2SD;
303 MSWD = 2.8; n = 11). The weighted average possesses a MSWD >1 and we interpret this to reflect
304 multiple zircon populations included within the weighted average calculation.

Sample CL1020 is a foliated granitoid with a weakly developed tectonic fabric. Fifty-two ablation analyses were measured from eighteen zircon crystals. Seven of these analyses (G2-1, G2-2, C5-1, H9-1, I1-2, Z4-1, and Z7 2) possessed significant common lead (1.5–4.6% f^{206}Pbc) and are not shown in Figs. 9a, b. Concordant $^{207}Pb/^{206}Pb$ ages (>95% concordance) possess a 150 Myr age range that likely reflects at least two disparate age components and each has likely undergone non-zero Pb-loss. CL imaging provides textural support for an inherited zircon component with the oldest zircon crystals corresponding to highly luminescent and resorbed zircon cores (Fig. 8c). The age of this older population is unclear as inherited zircon crystals are suspected to have undergone non-zero Pb-loss, however a weighted average $^{207}Pb/^{206}Pb$ age of the five oldest and most concordant (100 ± 2% concordance) zircon crystals that correspond to texturally distinct zircon zones represents a minimum age estimate of inherited zircon crystals at 2846 ± 7 (± 9 2SD; MSWD = 0.31; n = 5). The crystallization age of CL1020 is similarly open to interpretation as the younger age population likely includes inherited zircon crystals that have undergone non-zero Pb-loss; however a weighted average $^{207}Pb/^{206}Pb$ age of the fourteen most concordant (100 ± 2% concordance) zircon crystals corresponding to magmatically zoned zircon crystals provides our best estimate for the crystallization age of CL1020 at 2739 ± 10 (± 35 2SD; MSWD = 4.6; n = 14).

Sample CL1019 is a porphyritic monzogranite and possesses K-feldspar megacrysts (locally several cm in diameter) that distinguish this lithology from the other granitic phases in the field. Thirty-two ablations from sixteen zircon crystals were analyzed. Seven of these analyses (A10-1; B3-1; B10-1; C1-1; C4-1; E2-1; G10-1) contained significant concentrations of common Pb (1.9–2.7% f^{206}Pbc) and are not included in Figs. 10a, b. Two of the remaining twenty-five analyses are from zircon G1 and possess significantly older U-Pb ages (ca. 700 Myr). One of these analyses is near-concordant (96% concordance) and provides a $^{207}Pb/^{206}Pb$ age of 2671 ± 17 Ma. This zircon possesses a resorbed and highly luminescent centre and weakly luminescent margin. The textural and isotopic evidence suggest that this zircon is consistent with an inherited zircon component that was derived from Archean basement (e.g., CL098, CL109, and CL1020). All other CL1019 zircon analyses possess Proterozoic U-Pb ages and constrain a Model-2 York fit regression with an upper intercept age of 1948 ± 16 Ma and lower intercept age of 87 ± 150 Ma (MSWD = 13; n = 23). The high

MSWD reflects significant scatter about the discordia curve that is likely related to Pb-loss and a range of concordant U-Pb ages that may suggest multiple zircon populations were included in the regression. Concordant analyses are most likely to reflect the true crystallization age of the sample, and a weighted average $^{207}Pb/^{206}Pb$ age of the most concordant (>98% concordance) and Proterozoic zircon crystals is 1942 ± 14 Ma (± 35 2SD; MSWD = 3.3; n = 8).

Sample CL1021 is a quartz diorite intrusion adjacent to the Saza granodiorite (CL0975). Thirty ablation spots were analysed from 14 zircon grains. Three of these analyses (J1-23, J1-24, and D9-16) possessed large counts of common lead (1.5–2.1% $f^{206}Pbc$) and are not presented in the concordia plots (Figs. 10a, b) or discussed further. The remaining zircon crystals constrain a Model-2 York fit regression with an upper intercept age of 1907 ± 27 Ma and lower intercept age of 524 ± 140 Ma (MSWD = 5.8; n = 27). The dataset likely contains multiple zircon populations that are unresolvable within the assigned analytical uncertainties based on the 107 Myr range of near-concordant (>95% concordance) $^{206}Pb/^{238}U$ ages coupled with the high MSWD of the upper intercept age (Fig. 10b). Our best approximation to the crystallization of CL1021 is the upper intercept age of all the analyzed zircon crystals (except for those with excessive common lead and analysis J1-25 which plots significantly below discordia) at 1891 ± 17 (2SD = ?, MSWD = 4.8; n = 26).

Sample CL1022 is a massive gabbroic dike that is observed cross cutting a foliated granitoid (CL109). Twenty-one ablation spots from ten zircon crystals were analyzed and constrain a Model-2 York fit regression with an upper intercept age at 1880 ± 17 Ma and lower intercept at age 469 ± 81 Ma (MSWD = 4.9; n = 21). Near-concordant (>95% concordant) zircon crystals possess a 160 Myr range of $^{206}Pb/^{238}U$ ages and imply our dataset contain multiple zircon populations (Fig. 10b). Our best approximation of the crystallization age of CL1022 is the upper intercept age of all analyzed zircon crystals at 1880 ± 17 Ma (2SD = X, MSWD = 4.9; n = 21). Our interpreted crystallization age also constrains the timing of crystallization and provides a maximum possible age for deformation within the foliated granitoid (CL109).

4.4 LA-MC-ICP-MS Lu-Hf Zircon Results

Three Archean foliated granitoid samples (CL098, CL109 and CL1020) were selected for LA-MC-ICP-MS Lu-Hf isotopic analysis. These samples were chosen because of their unexpected

Archean age and their poorly constrained petrogenetic history. Only near-concordant (>95% concordance) zircon analyses were selected for Lu-Hf analysis and, in the majority of cases, the Lu-Hf ablation sites were centred over top of the pre-existing U-Pb ablation site (e.g., Fig. 8c). For zircon crystals where this was not possible (e.g., zircon growth zones were too thin), the Lu-Hf ablation site was repositioned adjacent to the U-Pb ablation site in what is assumed to be a coeval growth zone of the zircon. For ablation sites and CL images see Online Supplementary Figs. S1, S2 and S4. Reference material analyses and sample results are provided as Online Supplementary Table S8.

Zircon crystals incorporate a small amount of ^{176}Lu during crystallization which decays to ^{176}Hf. As a result, each measured $^{176}Hf/^{177}Hf$ ratio needs to be corrected for the interpreted crystallization age of the sample ($^{176}Hf/^{177}Hf_{initial}$). We approached this problem by using the $^{207}Pb/^{206}Pb$ age of the ablation site and the measured $^{176}Lu/^{177}Hf$ ratios to correct for the corresponding $^{176}Hf/^{177}Hf$ analysis. Normalizing $^{176}Hf/^{177}Hf_{initial}$ ratios to the $^{176}Hf/^{177}Hf$ value of the present-day bulk earth ($^{176}Hf/^{177}Hf_p = 0.28295$; Patchett and Tatsumoto, 1980) allows the calculation of εHf [$(^{176}Hf/^{177}Hf_{initial} / {}^{176}Hf/^{177}Hf_{present\ day\ earth}) \times 10^4$]. Crustal residence ages were calculated following a 2-stage model age approach. The calculated $^{176}Hf/^{177}Hf_{initial}$ ratio of the zircon at the time of growth ($^{207}Pb/^{206}Pb$ zircon age), and an average crustal $^{176}Lu/^{177}Hf$ ratio of 0.012 (Vervoort et al., 1999) were used to project back to the time of intersection with depleted mantle (with $^{176}Lu/^{177}Hf = 0.0384$, $^{176}Hf/^{177}Hf = 0.28325$: Chauvel and Blichert-Toft, 2001).

Forty-two Lu-Hf analyses were performed on fourteen zircon crystals from sample CL1020 (Fig. 11a). The $^{176}Hf/^{177}Hf$ analyses possess an approximately normal distribution and overlap within analytical uncertainty at the 2σ uncertainty level. Inherited zircon crystals possess identical $^{176}Hf/^{177}Hf_{initial}$ values (arithmetic average = 0.281010 ± 0.000045 at 2SD, n =26) within uncertainty but are generally lower than zircon crystals that are thought to represent crystallization of CL1020 at ca. 2.74 Ga (arithmetic average = 0.281032 ± 0.000029 at 2SD, n = 16).

Nineteen Lu-Hf analyses were performed on twelve concordant zircon crystals from CL098. $^{176}Hf/^{177}Hf$ analyses possess an approximately normal distribution and largely overlap within

analytical uncertainty at the 2σ uncertainty level (Fig. 11a). An arithmetic average of $^{176}Hf/^{177}Hf_{initial}$ for this sample is 0.281048 ± 0.000046 (2SD, n =19).

Fifteen Lu-Hf analyses were performed on ten concordant zircon crystals from CL109. One Lu-Hf analysis (H1-2) possesses an anomalously low $^{176}Hf/^{177}Hf$. The significance of this value is unclear and is not included in the following discussion, but is include on Figure 11. The remaining $^{176}Hf/^{177}Hf$ analyses possess a weakly bi-modal distribution (Fig. 11a). $^{176}Hf/^{177}Hf_{initial}$ values are largely within analytical uncertainty of each other (arithmetic average = 0.281047 ± 0.000025 at 2SD, n = 14) and the $^{176}Hf/^{177}Hf_{initial}$ values of CL098 (i.e., 0.281048) and CL1020 (i.e., 0.281032). The four oldest U-Pb analyses possess the highest $^{176}Hf/^{177}Hf_{initial}$ values and overlap with $^{176}Hf/^{177}Hf_{initial}$ values of interpreted inherited zircon cores from CL1020 at the 2σ uncertainty level.

4.5 Interpretation of complex inheritance, recrystallization, and Pb-loss systematics

Concordant LA-MC-ICP-MS U-Pb zircon analyses possess age ranges that exceed the analytical uncertainty of the individual measurements (e.g., near-concordant zircon crystals from CL1022 possess a 160 Myr range; Figs. 9 and 10). Reference material analyses, run as part of our standard-sample-standard bracketing protocol, overlap within analytical uncertainty and suggest that our analytical methodology cannot explain this age range and that real geologic scatter exists in our samples. The cause of the concordant U-Pb zircon age range can be constrained by integrating the U-Pb and Lu-Hf analyses with CL imaging for the same ablation pits. Previous studies provide empirical evidence to suggest that the U-Pb and Lu-Hf isotopic systems are decoupled during metamorphism (e.g., Gerdes and Zeh, 2009; Kemp et al., 2009; Whitehouse and Kemp, 2010). As a result, the $^{176}Hf/^{177}Hf_{initial}$ remains unchanged even for zircon crystals that exhibit U-Pb evidence for Pb-loss. The oldest $^{207}Pb/^{206}Pb$ ages from CL1020 correspond to highly luminescent and resorbed zircon cores that are interpreted to be inherited xenocrysts. Lu-Hf isotopic data supports this interpretation as $^{207}Pb/^{206}Pb$ ages <2.74 Ga possesses $^{176}Hf/^{177}Hf_{initial}$ ratios identical to zircon crystals with $^{207}Pb/^{206}Pb$ ages at ca. 2740 Ma, whereas inherited zircon crystals with $^{207}Pb/^{206}Pb$ ages >2.74 Ga possess generally less radiogenic $^{176}Hf/^{177}Hf_{initital}$ ratios. Our results possess considerable overlap, but generally less radiogenic, $^{176}Hf/^{177}Hf_{initial}$ values of inherited and magmatic zircon crystals suggest the source of inherited zircon crystals may have had a dissimilar Lu-Hf composition compared to the source of

magmatic zircon crystals. Conversely, younger zircon crystals that possess identical $^{176}Hf/^{177}Hf_{initial}$ ratios have likely undergone non-zero Pb-loss.

4.6 Lithogeochemistry Results

For lithogeochemical results see Online Supplementary Table S9 and Figures 13–15. Several samples (e.g., CL0956, CL0922) possess major element concentrations that total to less than 100%, which suggests some element(s) are not accounted for in the total calculations. Part of this discrepancy is explained by sulphur bearing phases (e.g., pyrite) that are not included in the major element total calculations and/or suggests that unanalysed elements (e.g., C) may also be present as minor components within several samples. Hydrothermal alteration and greenschist facies metamorphism are ubiquitous features of Lupa Terrane lithologies. Petrographic evidence such as partial to complete replacement of feldspars with sericite (± calcite) and partial to complete replacement of Fe-Mg minerals with amphibole (± chlorite, ± epidote, ± clinozoisite, ± titanite, ± calcite, ± opaques) are indicative of pervasive hydrothermal circulation (Fig. 6c). Chemical alteration is also inferred from large variations in certain major elements and Large Ion Lithophile Elements (LILE) which are considered to be mobile during hydrothermal alteration and metamorphism (e.g., Cs, Rb, Ba, Sr, and Pb; Grant, 2005). High Field Strength Elements (HFSE; e.g., Ti, Zr, Y, Nb, Hf, Ta, U, and Th), transitional elements (e.g., Ni, Cr, V, and Sc), and Rare Earth Elements (REE; e.g., La, Ce, Pr, Nd, Sm, Eu, Gd, Tb, Dy, Ho, Er, Tm, Yb, Lu) are least disturbed by hydrothermal processes (Floyd and Winchester, 1975; Winchester and Floyd, 1977). Thus, the following discussion is focused on trace elements that are considered to be more representative of protolith composition.

The trace element composition of the felsic lithologies can be qualitatively divided into three REE patterns and all phases share similar trace element patterns normalized to primitive mantle (Fig. 13a). Saza Granodiorite (CL1030; CL0975), granodiorite samples (CL0911; CL0921; CL0958), and porphyritic monzogranite (CL1029) possess Light Rare Earth Element (LREE) enrichment (La/Sm_{CN} = 5.2–11.7) and concave-up trends in the Medium and Heavy Rare Earth Elements (MREE and HREE, respectively). This pattern is in contrast to the REE pattern of foliated granite samples (CL098; CL0925; CL0947) which possess LREE enrichment (La/Sm_{CN} = 3.8–8.1), steeply dipping patterns towards the HREE (La/Yb_{CN} = 20.9–64.6), and minor negative Eu anomalies (Eu/Eu* = 0.7–

443 0.9). The third qualitatively distinct REE pattern is shown by the Ilunga Syenogranite (CL0931;
444 CL0932; CL0934; CL0959) which exhibits LREE enrichment (La/Sm_{CN} = 2.9–5.3), deep negative Eu
445 anomalies (Eu/Eu* = 0.08–0.36), and flat MREE and HREE patterns (Gd/Yb_{CN} = 0.9–1.3). On trace
446 element plots normalized to primitive mantle, all felsic phases possess LILE enrichment, gently-
447 dipping patterns towards the REE, and are characterized by large negative Nb and Ti anomalies
448 (Nb/Th_{CN} = 0.1–0.6; Ti/Sm_{CN} = 0.0–0.3; Fig. 13b).
449 The trace element compositions of the intermediate and mafic magmatic phases can be
450 qualitatively divided into two trace element groups (Figs. 13c and d). The diorite-gabbro suite
451 (CL1021; CL1022; CL0913; CL0923; CL0928; CL0957; CL0981; CL0984) possess LREE
452 enrichment (La/Sm_{CN} = 2.1–4.0) and gently-dipping slopes towards the HREE (La/Yb_{CN} = 3.0–19.9)
453 and minor positive Eu (i.e., Eu/Eu* = 1.5–1.1) anomalies. This distinctive REE profile is
454 complimented by LILE enrichment relative to HFSE, large negative Nb anomalies (Nb/Th_{CN} = 0.1–
455 0.2), and small negative Ti anomalies (Ti/Sm_{CN} = 0.2–1.2; only CL1022 has a positive Ti anomaly).
456 Two samples, CL0956 and CL0996, are dikes that cross cut foliated granitoids and the diorite-gabbro
457 suite, respectively and preserve their original clinopyroxene and orthopyroxene mineralogy. This
458 suggests that these two dikes post-date greenschist facies metamorphism and are potentially the
459 youngest rocks in the field area. These samples do not possess negative Nb or Ti anomalies which is a
460 consistent pattern shown by all other igneous phases in the sample suite. In addition, sample CL0956
461 possess an alkaline major element chemistry (K_2O wt. % + Na_2O wt. % = 6 % at 50 wt. % SiO_2),
462 which contrasts with the calc-alkaline nature of all the other magmatic phases. The timing and
463 petrogenetic significance of these late dikes is unclear.
464 *4.7 REE Modelling*
465 Our REE modelling used the non-modal melting equation of Shaw (1970) to assess whether
466 the diorite-gabbro suite could have formed from mantle sources with compositions typical of volcanic
467 arcs (following the approach of Dampare et al., 2008; Fig. 14). We chose primitive mantle (PM; Sun
468 and McDonough, 1989) and the depleted mid-ocean ridge basalt (DMM; McKenzie and O'Nions,
469 1991) as starting compositions and then calculated the REE concentrations of melts at increasing
470 degrees of partial melting. N-MORB and E-MORB (Sun and McDonough, 1989) are also plotted for

471 reference. Mineral/matrix partition coefficients are from McKenzie and O'Nions (1991); whereas
472 mineral modes and melt-modes for garnet lherzolite and spinel lherzolite are from Walter (1998) and
473 Kinzler, (1997), respectively.
474 Our results suggest that, even at low degrees of partial melting (i.e., <1%), the LREE
475 composition of the diorite gabbro suite cannot be explained by non-modal melting (Shaw, 1970) of
476 depleted mid-ocean ridge basalt or primitive mantle sources (Fig. 14a). Partial melting of spinel
477 lherzolite sources produce magmas with Sm/Yb ratios similar to the source, whereas partial melting of
478 a garnet lhzerolite with residual garnet produces melts with higher Sm/Yb ratios than the DMM-PM
479 "mantle" array (Fig. 14b). The diorite-gabbro suite of this study possesses Sm/Yb ratios greater than
480 even small degrees of partial melting of these potential mantle sources and is displaced from the
481 mantle array (Fig. 14b). Thus, the diorite-gabbro suite requires a REE enriched source (e.g., a more
482 differentiated source) and/or REE enrichment during magma-crust interaction. Furthermore, depleted
483 Nb/Ta (18–5) and enriched Zr/Hf ratios (50–39) relative to chondritic values (Nb/Ta = 17.6; Zr/Hf =
484 36.3) suggest these rocks are not mantle-derived magmas (Green, 2006). Volcanic arcs are thought to
485 possess depleted mantle sources that may be enriched in LILE and REE by a subduction component
486 and/or interaction with the crust (Pearce, 1996b), whereas continental arcs are known to have sources
487 that vary in composition from the upper mantle (i.e, fertile MORB mantle) to more enriched mantle
488 (Pearce and Parkinson, 1993). Alternatively, REE enrichment within the diorite-gabbro suite may be
489 due to melting a differentiated source in the lower crust. The exact source of the diorite-gabbro suite
490 is unclear because of a lack of petrogenetic constraints on melting processes, however our REE
491 modelling results are consistent with the trace element evidence (discussed in more detail below) that
492 supports the involvement of crust-magma interaction.
493
494 **5 Discussion**
495 *5.1 Archean granitoid petrogenesis*
496 Here we show that previously considered Proterozoic granites are in fact Archean (ca. 2.74
497 Ga). Furthermore, inherited zircon ages from sample CL1020 provide evidence for >2.74 Ga crust
498 beneath the Lupa Terrane. Other metamorphic belts surrounding the southern and eastern margins of

499 the Tanzanian Craton (e.g., Mozambique and Usagaran) also contain Archean crust (Muhongo et al.,
500 2001; Reddy et al., 2003; Sommer et al., 2003). These studies proposed that large portions of
501 metamorphic belts enveloping the Tanzanian Craton represent re-worked Archean crust and are
502 consistent with a growing number of deep seismic studies that demonstrate laterally extensive
503 Archean lithosphere underlying many Proterozoic accretionary orogens (Snyder, 2002). Alternatively,
504 Archean rocks may be unrelated to the Tanzanian Craton and may have been incorporated within
505 these metamorphic belts during accretion (Muhongo et al., 2001).
506 The SW extent of the Tanzanian cratonic margin is a subject of debate (e.g., Coolen, 1980;
507 Pinna et al., 2008). Manya (2011) proposed a possible location for the Tanzanian cratonic margin
508 based on Sm-Nd isotopic evidence. However, a sample from Manya (2011) was taken from an
509 outcrop in the Lupa Terrane and possessed an Archean Nd model age (i.e., 2688 Ma). That Archean
510 sample is ca. 150 km away from the newly proposed Tanzanian cratonic margin and Manya (2011)
511 interpreted the anomalous age as either a sliver of tectonically interleaved Archean material or re-
512 melting of Archean crust. Archean foliated granites in the Lupa Terrane are older (ca. 2740 Ma) than
513 Rb-Sr and K-Ar ages for the Tanzanian craton (2.4–2.6 Ga; Cahen et al., 1984) but are in good
514 agreement with re-worked Archean rocks in the Usagaran (ca. 2700 Ma; Reddy et al., 2003) and
515 Mozambique Belts [2740–2608 (Muhongo et al., 2001); 2970–2500 Ma (Sommer et al., 2003)] and
516 recent U-Pb zircon SIMS ages for the Tanzanian Craton (>3.6–2.6 Ga; Kabete et al., 2012a, b).
517 U-Pb and Lu-Hf isotopic evidence provides petrogenetic evidence that constrains the geologic
518 setting of the Archean granitoids. U-Pb zircon ages from CL098, CL109, and CL1020 record multiple
519 zircon populations that have undergone non-zero Pb-loss, nevertheless interpreted crystallization ages
520 are broadly within analytical uncertainty at ca. 2.74 Ga. The $^{176}Hf/^{177}Hf_{initial}$ ratios for interpreted
521 magmatic zircon crystals from all three samples are also largely within analytical uncertainty (2σ) and
522 suggests that all three foliated granitoid samples possess a homogeneous $^{176}Hf/^{177}Hf$ source.
523 Calculated εHf values (-2.2–2.8) plot lower than the depleted mantle (Griffin et al., 2000) and the
524 Neo-Mesoarchean mantle (Shirey et al., 2008) evolution curve (Fig. 11c). Juvenile melts (i.e., mantle
525 melts) are expected to possess $^{176}Hf/^{177}Hf_{initial}$ compositions that overlap with the $^{176}Hf/^{177}Hf$
526 composition of the mantle source and our results imply that foliated granitoids are not juvenile mantle

527 melts but likely formed from melting > 2.74 Ga crust (Fig. 11c). Melting was likely related to an
528 Archean volcanic-arc that is consistent with the subduction signature suggested by the Archean
529 granitoids trace element compositions (e.g., LREE enrichment; steeply dipping REE patterns;
530 negative Nb and Ti anomalies; Figs. 13e, f).

531 Crustal residence ages (CR) can be estimated from the calculated $^{176}Hf/^{177}Hf_{initial}$ values and
532 assuming a Lu-Hf composition of the mantle source (e.g., Shirey et al., 2008 and references therein).
533 Our two-stage Lu-Hf model ages are subject to large uncertainties because of ^{176}Lu decay constant
534 uncertainty, the poorly constrained Lu-Hf isotopic composition of the source, uncertainty regarding
535 the $^{207}Pb/^{206}Pb$ crystallization age of the samples and uncertainties on individual Lu-Hf measurements
536 (e.g., Davis et al., 2005). As a result, a range of model ages can be calculated from a single zircon
537 crystal (e.g., Whitehouse and Kemp, 2010). The arithmetic average CR age for samples CL098,
538 CL109, and CL1020 (not including inherited zircon crystals) is 3.1 Ga (± 0.9 Ga 2SD; n = 46). The
539 significance of this age is unclear because of the limitations described above, however depleted
540 mantle ages provide the first evidence for ≥ 3.1 Ga basement underlying the Lupa Terrane. The age of
541 this basement is consistent with Nd model ages (2.8–3.1 Ga) from the Tanzanian Craton, Usagaran
542 Belt, and the Mozambique Belt (Maboko, 1995; Maboko and Nakamura, 1996; Möller et al., 1998;
543 Kabete et al., 2012a).

544 CL1020 includes inherited zircon crystals with $^{207}Pb/^{206}Pb$ ages ca. 100 Myr older than the
545 interpreted crystallization age at ca. 2.74 Ga. The $^{176}Hf/^{177}Hf_{initial}$ values for suspected inherited zircon
546 crystals are generally lower (arithmetic average = 0.281010 ± 0.000045 at 2SD, n =26) but possess
547 significant overlap with zircon crystals that are thought to represent crystallization of CL1020 at ca.
548 2.74 Ga (arithmetic average = 0.281032 ± 0.000029 at 2SD, n = 16). Therefore, in addition to older
549 $^{207}Pb/^{206}Pb$ ages the suspected inherited zircon crystals appear to have a different $^{176}Hf/^{177}Hf$ source
550 than the magmatic zircon crystals. We propose that ca. >2.74 Ga zircon crystals represent an inherited
551 zircon component that may have been sourced from several protoliths of different ages or a single
552 protolith that crystallized at ca. 2.85 Ga and subsequently underwent non-zero Pb-loss to produce a
553 range of $^{207}Pb/^{206}Pb$ ages (Friend and Kinny, 1995). We favour the latter interpretation because the

554 $^{177}Hf/^{176}Hf_{initial}$ ratios of inherited zircon crystals are largely within analytical uncertainty of each other
555 and suggest a common $^{176}Hf/^{177}Hf_{initial}$ source.

556 Previous workers have suggested that Archean rocks within the Ubendian and Usagaran Belts
557 were tectonically interleaved during accretion (Muhongo et al., 2001; Manya, 2011). This hypothesis
558 seems unlikely in the Lupa Terrane where magmatic contacts are clearly observed between the
559 Archean and Paleoproterozoic granitoids (e.g., Fig. 4c). Seismic tomography models provide evidence
560 for re-worked Archean crust and upper lithosphere extending SW from the Tanzanian Craton to the
561 Bangweulu Block (see Fig. 2 of Begg et al., 2009). If correct, significant portions of the Ubendian
562 Belt may represent re-worked Archean crust. Our U-Pb and Lu-Hf support this hypothesis and we
563 propose that the Tanzanian cratonic margin is located at least 150 km SW from its currently accepted
564 position (Manya, 2011; Figs. 1). Our proposed model implies that Archean granitoids are present
565 between Lake Rukwa and currently known exposures of the Tanzanian Craton near the town of
566 Rungwa, but may be difficult to identify in the field as a result of reworking and/or the intrusion of
567 voluminous Paleoproterozoic granitoids.
568
569 *5.2 Paleoproterozoic Granitoid and Diorite-Gabbro Petrogenesis*
570 Ratios of highly incompatible elements have been shown to remain unchanged during large
571 degrees of partial melting or crystal fractionation (e.g., Pearce and Peate, 1995). Thus incompatible
572 elements can be used as tracers for magmatic processes. One important element for tracing subduction
573 zone processes is Nb, which is preferentially retained in the down-going slab within mineral phases
574 (e.g., rutile; Pearce and Peate, 1995). Nb depletions, such as those exhibited by Lupa Terrane intrusive
575 phases, are therefore characteristic of melts generated in volcanic arcs (Figs. 13d). The diorite-gabbro
576 suite also displays other trace element compositions that are typical of volcanic rocks erupting at
577 modern day volcanic-arcs. LREE enrichment (Hildreth and Moorbath, 1988), low TiO_2 contents (i.e.,
578 <2.0 wt. %; Pearce and Cann, 1973), large Ba/Ta and Ba/Nb ratios (i.e., >450, and >28, respectively;
579 Gill, 1981), low Y/Cr ratios (Pearce, 1982), high Th/Nb and Ce/Nb ratios (Saunders et al., 1988) all
580 suggest the diorite-gabbro suite are typical of calc-alkaline subduction-related (i.e., volcanic-arc)
581 magmas (Fig. 15). The diorite-gabbro suite also plots in the island-arc field of La-Sm-Th-Yb-Nb log-

582 transformed discrimination diagrams (Agrawal et al., 2008; Figs. 15e, f). Paleoproterozoic granitoids
583 also possess trace element characteristics typical of volcanic arcs (e.g., Nb and Ti depletions, high
584 Hf/Ta ratios range from 2–9; Pearce et al., 1984; Harris et al., 1986). Furthermore, the concave-up
585 pattern of the granodiorite samples (CL0975; CL0911; CL0921; CL0958) are typical of volcanic-arc
586 granites in which MREE strongly partition into hydrous phases, such as amphibole, during
587 crystallization (Pearce, 1996b; Fig. 13).
588 Volcanic-arc melts, oceanic or continental, typically originate as a result of partial melting of
589 depleted asthenosphere. Subduction processes (e.g., metasomatism in mantle wedge) and crust-
590 magma interaction (e.g., Melting-Assimilation-Segregation-Homogenization; Hildreth and Moorbath,
591 1988) can then modify the trace element composition of melt products (e.g., LILE and LREE
592 enrichment). Therefore, distinguishing source characteristics from crust-magma interaction is
593 difficult using trace element compositions alone (e.g., Davidson, 2005). Paleoproterozoic granitoids
594 and the diorite-gabbro suite are observed cross cutting Archean granitoids. Field observations and
595 inherited zircon crystals (e.g., CL1019) suggest that Paleoproterozoic magmatic phases likely
596 interacted with this evolved Archean crust (e.g., La/Yb_{cn} = 28.8–64.6) during emplacement. Crust-
597 magma interaction is typical of continental arcs and can explain the enriched LREE signature of Lupa
598 Terrane lithologies (REE modelling; Fig. 14). Large variations in LILE/HFSE ratios (e.g., Ba/La)
599 between broadly contemporaneous and spatially overlapping magmatic phases are more readily
600 explained by varying degrees of crustal-magma interaction and magmatic processes rather than
601 variability within melt sources (Hildreth and Moorbath, 1998). We therefore propose that trace
602 element compositions of Paleoproterozoic magmatic phases are typical of continental arcs that exhibit
603 evidence for crust-magma interaction, and that low Ti-Nb-Ta values argue against an intraplate
604 tectonic setting.
605
606 *5.3 Geochronologic Constraints on Deformation and Metamorphism*
607 The U-Pb geochronologic data from the current study constrains the absolute timing of
608 deformation events within the Lupa Terrane. At least three, temporally distinct, deformation events
609 (D1, D2, D3) are recognized in the field. The first deformation event (D1) is only developed within

610 the Archean granitoids. Undulating chlorite-rich bands separated by bands of K-feldspar, plagioclase,
611 and quartz give Archean granitoids a banded appearance. This tectonic fabric varies in intensity from
612 outcrop to outcrop but is consistently present across the field area. Archean foliated granitoids are
613 cross cut by non-foliated Paleoproterozoic granites, granodiorites, diorites, and gabbros. Our U-Pb
614 data broadly constrains the timing of D1 to between 2.72 and 1.96 Ga. Brittle-ductile mylonititc shear
615 zones (D2) crosscut all of the dated magmatic phases. This deformation event is economically
616 important as these structures are the primary host for Au mineralization (Lawley et al., in press). Our
617 U-Pb data constrains the timing of D2 to <1.89 Ga and is consistent with Re-Os dating of syn-
618 deformational pyrite at ca. 1.88 Ga (Lawley et al., in press). Greenschist facies metamorphism is
619 characteristic of the Au bearing shear zones and overprints all of the dated igneous phases. The timing
620 of greenschist facies metamorphism is therefore <1.89 Ga but likely related to D2 at ca. 1.88 Ga.
621 Gold- and pyrite-bearing quartz veins (D2) are locally crosscut by discrete brittle faults (D3). The
622 timing of D3 is not constrained, however the brittle nature of the faults is in contrast to the ductile
623 nature of deformation during D1 and D2 and suggests that D3 deformation may have occurred at
624 significantly shallower depths within the crust (Lawley et al., in press). The proposed temporally
625 distinct deformation events are only those that are readily distinguished in the field and it is expected
626 that Paleoproterozoic structures have been reactivated during tectonism that has continued to the
627 present day (Theunissen et al., 1996).

628 The U-Pb lower intercept ages reported as part of this study potentially provide evidence for
629 younger metamorphic overprints that broadly overlap with orogenic cycles recorded in the other
630 Ubendian Terranes (Boniface et al., 2012; Boniface and Schenk, 2012). For example, an imprecise U-
631 Pb lower intercept age for sample CL0911 (1126 ± 150 Ma) provides evidence for a Mesoproterozoic
632 Pb-loss event that is broadly equivalent to the Kibaran and/or Irumide orogenic cycles (de Waele et
633 al., 2009), whereas imprecise U-Pb lower intercept ages for samples CL109 (512 ± 140 Ma), CL1021
634 (524 ± 140 Ma) and CL1022 (469 ± 89 Ma), are broadly contemporaneous with the Pan African
635 Orogeny (Hanson, 2003). New U-Pb geochronology thus provides evidence for three orogenic cycles
636 that hitherto are unreported for the Lupa Terrane, but additional geochronology is required before
637 determine the significance and distribution of these younger metamorphic overprints.

638

639 *5.4 Geodynamic Model*

640 Paleoproterozoic magmatic rocks in the Lupa Terrane possess trace element compositions that
641 are typical of continental volcanic-arcs. Based on the geologic, geochronologic, and geochemical
642 evidence presented above we propose that the Lupa Terrane was a continental-arc during the
643 Paleoproterozoic. In our model, the Lupa Terrane represents the continental margin (i.e., the
644 Tanzanian cratonic margin) to which allochthonous terranes (i.e., other Ubendian Terranes) were
645 accreted. The 1.96–1.88 Ga magmatic events in the Lupa Terrane are younger than the 2.1–2.0 Ga
646 Ubendian tectonic phase but are in good agreement with the second Ubendian Tectonic phase at 1.9–
647 1.8 Ga. Current geochronologic constraints suggest that the Katuma-Ufipa-Lupa Terranes possess the
648 oldest ages (i.e., >1900 Ma) and are separated by the disparately younger Ubende-Mbozi Terrane (i.e.,
649 <1900 Ma). Our U-Pb crystallization ages (1960–1880 Ma) overlap with ages reported from each of
650 the lithotectonic terranes; however no ages reported in this study are comparable to the ca. 1860 Ma
651 eclogites in the Ubende Terrane (Boniface et al., 2012). The Katuma Terrane (1977–1900 Ma;
652 Boniface, 2009) lies along strike of the northwest trending Lupa Terrane and possess a similar
653 magmatic history that suggests both Terranes may have shared a similar tectono-magmatic evolution.

654 Recent ages constraining the temporal evolution of the Ubendian Belt are incompatible with
655 the existing tectonic model (Fig. 1b; Daly, 1988). For example, any geodynamic model must explain
656 the juxtaposition of greenschist facies metamorphism in the Lupa Terrane and contemporaneous
657 amphibolite-granulite facies metamorphism in the other Ubendian Terranes. The existing model of
658 wrench-dominated tectonics would require several hundred kilometres of lateral displacement to
659 explain this juxtaposition (Fig. 1b; Daly, 1988). Alternatively, subduction-related thrusting could have
660 brought high-grade metamorphic rocks in adjacent Ubendian Terranes to the same structural level as
661 the contemporaneous greenschist facies rocks comprising the Lupa Terrane. Our model would imply
662 that sub-horizontal lineations on the terrane-bounding shear zones may be related to strike-slip
663 reactivation of terrane sutures rather than Paleoproterozoic lateral accretion. The timing of this
664 juxtaposition is unclear as Mesoproterozoic, Neoproterozoic and Tertiary Rifting all likely contributed
665 to the current configuration of Ubendian Terranes (Boniface, 2009; Boniface et al., 2012; Boniface

666 and Schenk, 2012). The exact geodynamic evolution of the Ubendian Belt remains enigmatic and
667 requires additional constraints. Our results are however consistent with a protracted accretion history
668 during the 1.9–1.8 Ubendian tectonic phase (Boniface et al., 2009).
669
670 **6 Summary and Conclusions**
671 The magmatic history of the Lupa Terrane began in the Archean (ca. 2.74 Ga) with the
672 intrusion of evolved, calc-alkaline, and arc-type granites. Inherited U-Pb zircon ages and Lu-Hf zircon
673 isotopic evidence imply that these granites are the products of partial melting and incorporation of
674 substantially older crust (ca. 3.1 Ga). Archean granitoids were structurally deformed to produce a
675 weakly developed schistosity (D1; 2.74–1.96 Ga) and were then intruded by Paleoproterozoic (1.96–
676 1.88 Ga) calc-alkaline granitoids (syenogranites, monzogranites, and granodiorites) and dioritic-
677 gabbroic intrusions. Paleoproterozoic igneous lithologies are crosscut by Au-bearing and greenschist
678 facies shear zones (D2) that host the orogenic gold deposits of the Lupa Terrane. Based on the U-Pb,
679 Lu-Hf, trace element and field evidence presented above we propose:
680 • At least a 150km SW extension of the Tanzanian cratonic margin to the Rukwa escarpment.
681 Our results are consistent with seismic tomography studies that provide evidence for Archean
682 upper lithosphere extending SW from the Tanzanian Craton to the Bangweulu Block (Begg et
683 al., 2009).
684 • That Paleoproterozoic magmatic activity possesses trace element characteristics that are
685 analogous to modern-day continental arcs.
686 • That the Lupa Terrane acted as the continental margin onto which the other Ubendian
687 Terranes were accreted during the Paleoproterozoic. Inherited zircon crystals, trace elements
688 and REE modelling suggest the diorite-gabbro suite underwent magma-crust interaction,
689 which is consistent with a continental arc setting.
690 • That Paleoproterozoic eclogites with MORB-like chemistry (Boniface et al., 2012) imply
691 subduction and thrusting were important accretion processes in contrast to the wrench-
692 dominated tectonics proposed by Daly (1988). Thrusting could also explain the juxtaposition

of contemporaneous greenschist facies metamorphism in the Lupa with amphibolite-granulite facies metamorphism characteristic of the other Ubendian Terranes.

Acknowledgements

Funding and support was provided by a Durham Doctoral Fellowship at Durham University and student research grant from the Society of Economic Geologists to CJML. Helio Resource Corp. kindly provided funding, and access to drill core/exploration licenses for sampling. This work benefitted from discussion with Nelson Boniface and Bruce Kjarsgaard. Two anonymous reviewers also greatly improved the manuscript.

Electronic Supplement: Analytical Methods

Zircon Mineral Separation

Zircon crystals were separated from their host rock by crushing ~5 kg of rock in a jaw crusher and pulverizing in a disc mill before passing the sample through a 355 μm sieve. Samples were then placed on a Rogers shaking table and the heavy fraction dried (at 60ºC) before passing through a Frantz isodynamic magnetic separator. The non-magnetic fractions of each sample were then density separated using methylene iodide before handpicking, under ethanol, of the most crack- and inclusion-free grains.

U-Pb Zircon ID-TIMS

All the analyzed zircon crystals have undergone the "chemical abrasion" (thermal annealing and subsequent leaching) pre-treatment technique (Mattinson, 2005) for the effective elimination of Pb-loss. This involved placing zircon crystals in a muffle furnace at 900 ± 20°C for ~60 hours in quartz beakers before being transferred to 3ml Hex Savillex beakers, placed in a Parr vessel, and leached in a ~5:1 mix of 29M HF + 30% HNO3 for 12 hours at ~180°C. The acid solution was removed, and fractions were rinsed in ultrapure H2O, fluxed on a hotplate at ~80°C for an hour in 6 M HCl, ultrasonically cleaned for an hour, and then placed back on the hotplate for an additional 30 min. The HCl solution was removed and the fractions (single zircon crystals or fragments) were selected, photographed (in transmitted light) and again rinsed (in ultrapure acetone) prior to being

721 transferred to 300 µl Teflon FEP microcapsules and spiked with a mixed ^{233}U–^{235}U–^{205}Pb tracer.
722 Zircon was dissolved in ~120 µl of 29 M HF with a trace amount of 30% HNO3 with microcapsules
723 placed in Parr vessels at ~220°C for 48 hours, dried to fluorides, and then converted to chlorides at
724 ~180°C overnight. U and Pb for all minerals were separated using standard HCl-based anion-
725 exchange chromatographic procedures.
726 Isotope ratios were measured at the NERC Isotope Geosciences Laboratory (NIGL), UK,
727 using a Thermo-Electron Triton Thermal Ionisation Mass-Spectrometer (TIMS). Pb and U were
728 loaded together on a single Re filament in a silica-gel/phosphoric acid mixture. Pb was measured by
729 peak-hopping on a single SEM detector. U isotopic measurements were made in static Faraday mode.
730 Age calculations and uncertainty estimation (including U/Th disequilibrium) was based upon the
731 algorithms of Schmitz and Schoene (Schmitz and Schoene, 2007).
732 *U-Pb Zircon LA-MC-ICP-MS*
733 Laser Ablation Multi-Collector Inductively Coupled Plasma Mass Spectrometry (LA-MC-
734 ICP-MS) was conducted at the NERC Isotope Geoscience Laboratory (NIGL). Zircon mineral
735 separates were mounted in epoxy, polished, and imaged using cathodoluminesence (CL) on a
736 scanning electron microscope (SEM) at the British Geological Survey (with the exception of CL098
737 which was prepared at the School of Natural Sciences, Trinity College Dublin). CL imaging provided
738 textural information that assisted zircon targeting. Zircon crystals were ablated using a New Wave
739 Research UP193SS Nd:YAG laser ablation system and an in-house built low-volume rapid washout
740 ablation cell. Ablated material was transported from the ablation cell using a continuous flow of He
741 gas to a Nu Plasma MC-ICP-MS equipped with a multi-ion-counting array. ^{207}Pb, ^{206}Pb and ^{204}Pb+Hg
742 isotopes were measured on ion counters whereas U and Tl isotopes and ^{202}Hg were measured using
743 faraday cups. Data were collected using the Nu Instruments time resolved analysis software. Prior to
744 analysis, the MC-ICP-MS was tuned and gains were measured using a Tl-^{235}U solution co-aspirated
745 using a Nu Instruments DSN-100 desolvating nebuliser. At the start of each run an instrument zero
746 was measured for 30s and was followed by three 30s ablations of three reference materials. The
747 internationally recognized 91500 reference zircon (Weidenbeck et al., 1995) was used as the primary
748 reference material, whereas Plešovice (Sláma et al., 2008) and GJ-1 (Jackson et al., 2004) were used

as validation materials. All three matrix matched materials were used to monitor instrumental drift and 91500 was used to correct for instrumental drift. The nine standard ablations were followed by ca. twelve 30s sample ablations. Once data stability had been established replicates were dropped to one to two for each reference materials. All ablations used a 25–30 μm static spot at 5 Hz, and a fluence of 2.7 J/cm^2. During each analysis the co-aspirated Tl-^{235}U solution was used to correct for instrumental mass bias and plasma induced elemental fractionation. The interference of ^{204}Hg on ^{204}Pb was monitored and corrected for by simultaneously measuring ^{202}Hg and assuming a ^{204}Hg/^{202}Hg = 0.229887. U-Pb data were processed using an in-house spread sheet at NIGL.

All presented ^{206}Pb/^{238}U dates (ID-TIMS and LA-ICP-MS) are calculated using the ^{238}U and ^{235}U decay constants of Jaffey et al. (Jaffey et al., 1971). The consensus value of ^{238}U/^{235}U = 137.818 ± 0.045 (Hiess et al., 2012) was used in the data reduction calculations. Using this more accurate value with its associated uncertainty estimate has the effect of lowering ^{207}Pb/^{206}Pb dates at c. 2 Ga by 0.8 ± 0.6 Myr, compared to ^{207}Pb/^{206}Pb dates calculated using the consensus value of ^{238}U/^{235}U = 137.88. For U–Pb dates of this age the ^{206}Pb/^{238}U dates are the most precise and robust. In contrast, the ^{207}Pb-based dates (^{207}Pb/^{235}U and ^{206}Pb/^{207}Pb) are considerably less precise and hence are only used to assess concordance of the U–Pb (zircon) systematics.

References

Agrawal, S., Guevara, M., and Verma, S., 2008. Tectonic discrimination of basic and ultrabasic volcanic rocks through log-transformed ratios of immobile trace elements. International Geology Review 50, 1057–1079.

Begg, G.C., Griffin, W.L., Natapov, L.M., O'Reilly, S.Y., Grand, S.P., O'Neill, C.J., Hronsky, J.M.A., Poudjom Djomani, Y., Swain, C.J., Deen, T., and Bowden, P., 2009. The lithospheric architecture of Africa: seismic tomography, mantle petrology, and tectonic evolution. Geosphere 5, 23–50.

777 Boniface, N., 2009. Eburnian, Kibaran, and Pan-African metamorphic events in the Ubendian Belt of
778 Tanzania; petrology, zircon and monazite geochronology. Unpublished PhD thesis, Kiel
779 University, Germany, 110 p.
780
781 Boniface, N., Schenk, V., and Appel, P., 2012. Paleoproterozoic eclogites of MORB-type chemistry
782 and three Proterozoic orogenic cycles in the Ubendian Belt (Tanzania): evidence from monazite
783 and zircon geochronology, and geochemistry. Precambrian Research 192–195, 16–33.
784
785 Boniface, N., and Schenk, V., 2012. Neoproterozoic eclogites in the Paleoproterozoic Ubendian Belt
786 of Tanzania: evidence for a Pan-African suture between the Bangweulu Block and the Tanzania
787 Craton. Precambrian Research 208–211, 72–89.
788
789 Boven, A., Theunissen, K., Skylarov, E., Klerkx, J., Melnikov, A., Mruma, A., and Punzalan, L.,
790 1999. Timing of exhumation of a high-pressure mafic granulite Terrane of the Paleoproterozoic
791 Ubende Belt (west Tanzania). Precambrian Research 93, 119–137.
792
793 Brock, P.W.G., 1963. The Mbozi syenite-gabbro complex. Unpublished PhD Thesis, University of
794 Leeds, UK, 261 p.
795
796 Cahen, L., Snelling, N.J., Delhal, J., and Vail, J., 1984. The geochronology and evolution of Africa,
797 Clarendon Press, Oxford.
798
799 Chauvel, C., and Blichert-Toft, J., 2001. A hafnium isotope and trace element perspective on melting
800 of the depleted mantle. Earth and Planetary Science Letters 190, 137–151.
801
802 Collins, A.S., Reddy, S.M., Buchan, C., and Mruma, A., 2004. Temporal constraints on
803 Palaeoproterozoic eclogite formation and exhumation (Usagaran, Orogen, Tanzania). Earth and
804 Planetary Science Letters 224, 175–192.

Coolen, J.J.M.M.M., 1980. Chemical petrology of the Furua Granulite Complex, southern Tanzania: Unpublished PhD thesis, 13Vrije University, Amsterdam, GUA pap. Geol., Ser. 1, 258 p.

Daly, M.C., 1988. Crustal shear zones in central Africa; a kinematic approach to Proterozoic tectonics. Episodes 11, 5–11.

Dampare, S.B., Shibata, T., Asiedu, D.K., Osae, S., and Banoeng-Yakubo, B., 2008. Geochemistry of Paleoproterozoic metavolcanic rocks from the southern Ashanti volcanic belt, Ghana: Petrogenetic and tectonic setting implications: Precambrian Research 162, 403–423.

Davidson, J.P., Hora, J.M., Garrison, J.M., and Dungan, M.A., 2005. Crustal forensics in arc magmas. Journal of Volcanology and Geothermal Research 140, 157–170.

Davis, D.W., Amelin, Y., Nowell, G.M., and Parrish, R.R., 2005. Hf isotopes in zircon from the western Superior Province, Canada: Implications for Archean crustal development and evolution of the depleted mantle reservoir. Precambrian Research 140, 132–156.

de Waele, B., Fitzsimons, I.C.W., Wingate, M.T.D., Timbo, F., Mapani, B., and Belousova, E.A., 2009. The geochronological framework of the Irumide Belt: A prolonged crustal history along the margin of the Bangweulu Craton. American Journal of Science 309, 132–187.

Dodson, M.H., Cavanagh, B.J., Thatcher, E.C., and Aftalion, M., 1975. Age limits for the Ubendian metamorphic episode in northern Malawi. Geological Magazine 112, 403–410.

Friend, C.R.L., and Kinny, R.D., 1995. New evidence for protolith ages of Lewisian granulites, northwest Scotland. Geology 23, 1027–1030.

833 Floyd, P.A., and Winchester, J.A., 1975. Magma type and tectonic setting discrimination using
834 immobile elements. Earth and Planetary Science Letters 27, 211–218.
835
836 Gabert, G. and Wendt, I. 1974. Datierung von granitischen Gesteinen im Dodoman- und Usagaran-
837 System und in der Ndembera-Serie (Tanzania). Geologische Jahrbuch, B 11, 3–55.
838
839 Gallagher, D.R., 1939. Preliminary account of the geology of a portion of Lupa goldfield. Economic
840 Geology 34, 306–323.
841
842 Gerdes, A., and Zeh, 2009. Zircon formation versus zircon alteration – new insights from the
843 combined U-Pb and Lu-Hf in-situ LA-ICP-MS analyses, and consequences for the
844 interpretation of Archean zircon from the Central Zone of the Limpopo Belt. Chemical Geology
845 261, 230–243.
846
847 Gill, J.B., 1981. Orogenic Andesites and Plate Tectonics, Springer-Verlag, Berlin.
848
849 Grant, J.A., 2005. Isocon analysis; a brief review of the method and applications. Physics and
850 Chemistry of the Earth, Parts A/B/C, 30, 997–1004.
851
852 Grantham, D.R., 1931. Lupa river goldfield. Mining Magazine 45, 265–276.
853
854 Grantham, D.R., 1932. Lupa goldfield. Bulletin of the Geological Survey of Tanganyika 3, 34 p.
855
856 Grantham, D.R., 1933. The eastern extension of Lupa goldfield. Geological Survey of Tanganyika,
857 short paper 11, 9 p.
858

Green, N.L., 2006. Influence of slab thermal structure on basalt source regions and melting conditions: REE and HFSE constraints from the Garibaldi volcanic Belt, northern Cascadia subduction system. Lithos 87, 23–49.

Griffin, W.L., Pearson, N.J., Belousova, E., Jackson, S.E., van Achterbergh, E., O'Reilly, S.Y., Shee, S.R., 2000. The Hf isotope composition of cratonic mantle: LAM-MC-ICPMS analysis of zircon megacrysts in Kimberlites. Geochimica et Cosmochimica Acta 64, 133–147.

Hanson, R.E., 2003, Proterozoic geochronology and tectonic evolution of southern Africa, in: Yoshida, M., Windley, B.F., and Dasgupta, S., (Eds.), Proterozoic East Gondwana: Supercontinent Assembly and Breakup, Geological Society, London, Special Publications 206, pp. 427–463.

Harris, J.F., 1961. Summary of geology of Tanganyika. Geological Survey of Tanganyika Memoir 1, 64–67.

Harris, N.B.W., Pearce, J.A., and Tindle, A.G., 1986. Geochemical characteristics of collision-zone magmatism, in: Coward, M.P., and Ries, A.C., (Eds.), Collision Tectonics, Geological Society Special Publications 19, pp. 51–81.

Hiess, J., Condon, D. J., McLean, N., and Noble, S. R., 2012. $^{238}U/^{235}U$ Systematics in Terrestrial Uranium-Bearing Minerals. Science 335 (no. 6076), 1610-1614.

Hildreth, W., and Moorbath, S., 1988. Crustal contributions to arc magmatism in the Andes of central Chile. Contributions to Mineralogy and Petrology 98, 455–489.

885 Jackson, S.E., Pearson, N.J., Griffin, W.L., and Belousova, E.A., 2004. The application of laser
886 ablation-inductively coupled plasma-mass spectrometry to in situ U-Pb zircon geochronology.
887 Chemical Geology 211, 47–69.
888
889 Jaffey, A. H., Flynn, K. F., Glendenin, L. E., Bentley, W. C., and Essling, A. M., 1971. Precision
890 measurement of half-lives and specific of ^{235}U and ^{238}U. Physics Reviews C4, 1889-1906.
891
892 Kabete, J.M., McNaughton, N.J., Groves, D.I., and Mruma, A.H., 2012a. Reconnaissance SHRIMP
893 U-Pb zircon geochronology of the Tanzania Craton: Evidence for Neoarchean granitoid-
894 greenstone belts in the Central Tanzania Region and the Southern East African Orogen.
895 Precambrian Research 216–219, 232–266.
896
897 Kabete, J.M., Gorves, D.I., McNaughton, N.J., and Mruma, A.H., 2012b, A new tectonic and
898 temporal framework for the Tanzanian Shield: Implications for gold metallogeny and
899 undiscovered endowment. Ore Geology Reviews 48, 88–124.
900
901 Kemp, A.I.S., Foster, G.L., Scherstén, A., Whitehouse, M.J., Darling, J., and Storey, C., 2009.
902 Concurrent Pb-Hf isotope analysis of zircon by laser ablation multi-collector ICP-MS, with
903 implications for the crustal evolution of Greenland and the Himalayas. Chemical Geology 261,
904 244–260.
905
906 Kilembe, E.A., and Rosendahl, B.R., 1992. Structure and stratigraphy of the Rukwa rift.
907 Tectonophysics 209, 143–158.
908
909 Kimambo, R.H.N., 1984. Mining and mineral prospects in Tanzania, Eastern Africa Publications Ltd.,
910 Arusha.
911

912 Kinzler, R.J., 1997. Melting of mantle peridotite at pressures approaching the spinel to garnet
913 transition: applications to mid-ocean ridge basalt petrogenesis. Journal of Geophysical
914 Research 102, 853–874.
915
916 Kröner, A., Muhongo, S., Hegner, E., and Wingate, M.T.D., 2003. Single-zircon geochronology and
917 Nd isotopic systemtics of Proterozoic high-grade rocks from the Mozambique belt of southern
918 Tanzania (Masasi area): implications for Gondwana assembly. Journal of the Geological
919 Society 160, 745–757.
920
921 Lawley, C.J.M., 2012. Geochronology and structure of the Lupa goldfield, Tanzania. Unpublished
922 PhD thesis, Durham University, Durham, UK, 219 p.
923

924 Lawley, C.J.M., Selby, D., and Imber, J., in press, Re-Os Molybdenite, pyrite and chalcopyrite
925 geochronology, Lupa Goldfield, SW Tanzania: Tracing metallogenic time scales at mid-crustal
926 shear zones hosting orogenic Au deposits: Economic Geology.

927 Lawley, C.J.M., Imber, J., and Selby, D., in press, Structural controls on orogenic Au-mineralization
928 along a non-Andersonian fault/shear zone system: Lupa goldfield, SW Tanzania: Economic
929 Geology.

930
931 LeMaitre, R.W., Streckeisen, A., Zanettin, B., Le Bas, M.J., Bonin, B., and Bateman, P., 2002.
932 Igneous rocks: a classification and glossary of terms; recommendations of the International
933 Union of Geological Sciences Subcommission on the systematics of igneous rocks, Cambridge
934 University Press, Cambridge.
935

936 Lenoir, J.L., Liégeois, J.P., Theunissen, K., and Klerkx, J., 1994. The Palaeoproterozoic Ubendian
937 shear Belt in Tanzania: geochronology and structure. Journal of African Earth Sciences 19,
938 169–184.
939
940 Ludwig, K.A. 2008. User's Manual for Isoplot 3.6, A Geochronological Toolkit for Microsoft Excel.
941 Berkeley Geochronology Center Special Publication No. 4, 77 p.
942
943 Maboko, M.A.H., 1995. Neodymium isotopic constraints on the protolith ages of rocks involved in
944 Pan-African tectonism in the Mozambique Belt of Tanzania. Journal of the Geological Society
945 152, 911–916.
946
947 Maboko, M.A.H., and Nakamura, E., 1996. Nd and Sr isotopic mapping of the Archaean-Proterozoic
948 boundary in southeastern Tanzania using granites as probes for crustal growth. Precambrian
949 Research 77, 105–115.
950
951 Manya, S., 2011. Nd-isotope mapping of the Archean-Proterozoic boundary in southwestern
952 Tanzania: implication for the size of the Archean Tanzanian Craton. Gondwana Research 20,
953 325–334.
954
955 Manya, S., 2012. SHRIMP zircon U-Pb dating of the mafic and felsic intrusive rocks of the Saza area
956 in the Lupa goldfields, southwestern Tanzania: Implications for gold mineralization: Natural
957 Science 4, 724–730.
958
959 Marobhe, I., 1989. Interpretation of aerogeophysical anomalies of southwestern Tanzania. Geological
960 Survey of Finland Bulletin 350, 72 p.
961

962 Mattinson, J.M., 2005. Zircon U-Pb chemical abrasion ("CA-TIMS") method: combined annealing
963 and multi-step partial dissolution analysis for improved precision and accuracy of zircon ages.
964 Chemical Geology 220, 47–66.
965
966 McConnell, R.B., 1950. Outline of the geology of Ufipa and Ubende. Geological Survey of
967 Tanganyika Bulletin 19, 62 p.
968
969 McKenzie, D., and O'Nions, R.K., 1991. Partial melt distribution from inversion of rare earth element
970 concentrations. Journal of Petrology 32, 1021–1091.
971
972 Meschede, M., 1986. A method of discriminating between different types of mid-ocean ridge basalts
973 and continental tholeiites with the Nb-Zr-Y diagram. Chemical Geology 56, 207–218.
974
975 Mnali, S.R., 1999. Palaeoproterozoic felsic magmatism and associated gold-quartz vein
976 mineralization in the western part of the Lupa goldfield, south-western Tanzania. Unpublished
977 PhD thesis, University of Dar es Salaam, Tanzania 198 p.
978
979 Mnali, S.R., 2002. Tectonic setting of gabbroic rocks in the western part of the Lupa gold field, south-
980 west Tanzania. Tanzanian Journal of Science 28, 99–113.
981
982 Möller, A., Appel, P., Mezger, K., and Schenk, V., 1995. Evidence for a 2 Ga subduction zone:
983 eclogites in the Usagaran Belt of Tanzania. Geology 23, 1067–1070.
984
985 Möller, A., Mezger, K., and Schenk, V., 1998. Crustal age domains and the evolution of the
986 continental crust in the Mozambique Belt of Tanzania: combined Sm-Nd, Rb-Sr, and Pb-Pb
987 isotopic evidence. Journal of Petrology 39, 749–783.
988

989 Muhongo, S., Tuisku, P., Mnali, S., Temu, E., Appel, P., and Stendal, H., 2001. High-pressure
990 granulite-facies metagabbros in the Ubendian Belt of SW Tanzania: preliminary petrography
991 and P-T estimates. Journal of African Earth Sciences 34, 279–285.
992
993 Nowell, G.M., and Parrish, R.R., 2001, Simultaneous acquisition of isotope compositions and
994 parent/daughter ratios by non-isotope dilution-mode plasma ionisation multi-collector mass
995 spectrometry (PIMMS), in: Holland, G. and Tanner, S.D., (Eds.), Plasma Source Mass
996 Spectrometry: The New Millenium. Royal Chemical Society, Special Publication 267, pp. 298–
997 310.
998
999 Patchett, P.J., and Tatsumoto, M., 1980. Halfnium isotope variations in oceanic basalts. Geophysical
1000 Research Letters 7, 1077–1080.
1001
1002 Pearce, J.A., and Cann, J.R., 1973. Tectonic setting of basic volcanic rocks determined using trace
1003 element analysis. Earth and Planetary Science Letters 19, 290–300.
1004
1005 Pearce, J.A., 1982. Trace element characteristics of lavas from destructive plate boundaries, in:
1006 Thorpe, R.S., (Ed.), Andesites. Wiley, New York, pp. 525–548.
1007
1008 —, 1983. Role of the subcontinental lithosphere in magma genesis at active continental margins, in:
1009 Hawkesworth, C.J., and Norry, M.J., (Eds.), Continental Basalts and Mantle Xenoliths.
1010 Cheshire, UK, Shiva Press Ltd., pp. 230–249.
1011
1012 Pearce, J.A., Harris, N.B.W., and Tindle, A.G., 1984. Trace element discrimination diagrams for the
1013 tectonic interpretation of granitic rocks. Journal of Petrology 25, 956–983.
1014
1015 Pearce, J.A., and Parkinson, I.J., 1993. Trace element models for mantle melting: application to
1016 volcanic arc petrogenesis, in: Prichard, H.M., Alabaster, T., Harris, N.B.W., and Neary, C.R.,

(Eds.), Magmatic Processes and Plate Tectonics. Geological Society Special Publication 76, pp. 373–403.

Pearce, J.A., and Peate, D.W., 1995. Tectonic implications of the composition of volcanic arc magmas. Annual Review of Earth and Planetary Sciences 23, 251–285.

Pearce, J.A., 1996a. A user's guide to basalt discrimination diagrams, in: Wyman, D.A., (Ed.), Trace Element Geochemistry of Volcanic Rocks: Applications for Massive Sulphide Exploration. Geological Association of Canada, Short Course Notes 12, pp. 79–113.

—, 1996b. Sources and settings of granitic rocks. Episodes 19, 120–125.

Pietranik A.B., Hawkesworth C.J., Storey C.D., Kemp A.I.S., Sircombe K.N., Whitehouse M.J., and Bleeker W., 2008. Episodic mafic crust formation from 4.5 to 2.8 Ga: New evidence from detrital zircons, Slave craton, Canada. Geology 36, 875–878.

Pinna, P., Muhongo, S., Mcharo, A., Le Goff, E., Deschamps, Y., Ralay, F., Milesi, J.P., 2008. Geology and mineral map of Tanzania. Geological Survey of Tanzania, Dodoma.

Priem, H.N.A., Boelrijk, N.A.I.M., Hebeda, E.H., Verdurmen, E.A.T., Verschure, R.H., Oen, I.S., and Westra, L., 1979. Isotopic age determinations on granitic and gneissic rocks from the Ubendian-Usagaran system in southern Tanzania. Precambrian Research 9, 227–239.

Reddy, S.M., Collins, A.S., and Mruma, A., 2003. Complex high-strain deformation in the Usagaran Orogen, Tanzania: structural setting of Palaeoproterozoic eclogites. Tectonophysics 375, 01–123.

Reddy, S.M., and Evans, D.A.D., 2009. Palaoproterozoic supercontinents and global evolution: correlations from core to atmosphere, in: Reddy, S.M., Mazumder, R., Evans, R., and Collins, D.A.D., (Eds.), Palaeoproterozoic Supercontinents and Global Evolution. Geological Society Special Publications 232, pp. 1–26.

Ring, U., 1993. Aspects of the kinematic history and mechanisms of superposition of the Proterozoic mobile Belts of eastern Central Africa (northern Malawi and southern Tanzania). Precambrian Research 62, 207–226.

Ring, U., Kröner, A., and Toulkeridis, T., 1997. Palaeoproterozoic granulite-facies metamorphism and granitoid intrusions in the Ubendian-Usagaran Orogen of northern Malawai, east-central Africa. Precambrian Research 85, 27–51.

Sango, P.M., 1988. Structural and lithological controls of gold mineralization in the Lupa goldfield, Tanzania, in: Ho, S.E., and Groves, D.I., (Eds.), Recent Advances in Understanding Precambrian Gold Deposits. Geology Department and University Extension, The University of Western Australia, Publication No. 12, pp. 99–109.

Saunders, A.D., Norry, M.J., and Tarney, J., 1988. Origin of MORB and chemically-depleted mantle reservoirsL: trace element constraints. Journal of Petrology (Special Lithosphere Issue), 415–445.

Schandelmeier, H., 1983. The geochronology of post-Ubendian granitoids and dolerites from the Mambwe area, northern province, Zambia. Report Institute Geological Sciences 83, 40–46.

Shaw, D.M., 1970. Trace element fractionation during anatexsis. Geochimica Cosmochimica Acta 34, 237–243.

Schmitz, M.D., and Schoene, B., 2007. Derivation of isotope ratios, errors, and error correlations for U-Pb geochronology using ^{205}Pb-^{235}U(^{233}U)-spiked isotope dilution thermal ionization mass spectrometric data. Geochemistry, Geophysics, Geosystems 8, 20 p.

Shervais, J.W., 1982. Ti-V plots and the petrogenesis of modern ophiolitic lavas. Earth and Planetary Science Letters 59, 101–118.

Shirey, S.B., Kamber, B.S., Whitehouse, M.J., Mueller, P.A., and Basu, A.R., 2008. A review of the isotopic and trace element evidence for mantle and crustal processes in the Hadean and Archaean: implications for the onset of plate tectonic subduction, in: Condie, K.C., and Pease, V.L., (Eds.), When did Plate Tectonics Start on Earth?, Geological Society of America, Memoir 440, pp. 1–29.

Simpson, R., 2012. NI 43-101 mineral resource estimate update for the Saza-Makongolosi Gold Project, Tanzania. Unpublished SRK consulting report, 217 p.

Sláma, J., Košler, J., Condon, D.J., Crowley, J.L., Gerdes, A., Hanchar, J.M., Horstwood, M.S.A., Morris, G.A., Nasdala, L., Norberg, N., Schaltegger, U., Schoene, B., Tubrett, M.N., Whitehouse, M.J., 2008. Plesovice zircon — a new natural reference material for U-Pb and Hf isotopic microanalysis. Chemical Geology 249, 1–35.

Smirnov, V., Pentel'kov, V., Tolochko, V., Trifan, M., and Zhukov, S., 1973. Geology and minerals of the central part of the western rift. Report on Geological Mapping, Mineral and Resource Division, Dodoma, Tanzania, 333 p.

Sommer, H., Kröner, A., Hauzenberger, C., Muhongo, S., and Wingate, M.T.D., 2003. Metamorphic petrology and zircon geochronology of high-grade rocks from the central Mozambique Belt of

Tanzania: crustal recycling of Archean and Paleoproterozoic material during the Pan-African orogeny. Journal of Metamorphic Geology 21, 915–934.

Sommer, H., Kröner, A., Muhongo, S., and Hauzenberger, C., 2005. Ages for post-Usagaran granitoid and rhyolitic rocks, Tanzania. South African Journal of Geology 108, 247–256.

Sun, S.S., and McDonough, W.F., 1989. Chemical and isotopic systematics of ocean basalts; implications for mantle composition and processes, in: Saunders, A.D., Norry, M.J., (Eds.), Magmatism in Ocean Basins. Geological Society of London Special Publication 42, pp. 313–345.

Sutton, J., Watson, J., and James, T.C., 1954. A study of the metamorphic rocks of Karema and Kungwe bay, western Tanganyika. Bulletin of the Geological Survey of Tanganyika 22, 70 p.

Snyder, D.B., 2002. Lithospheric growth at margins of cratons. Tectonophysics 355, 7–22.

Teale, E.O., Eades, N.W., Harkin, D.A., Harpum, J.R., and Horne, R.G., 1935. Brief explanation of the geology of Irambo area, quarter degree sheet 245, Geological Survey of Tanganyika, Dodoma.

Theunissen, K., Lenoir, J. L., Liégeois, J-P., Delvaux, D., and Mruma, A., 1992. Empreinte pan-africaine majeure dans la chaine ubendienne de Tanzanie sud-occidentale: geochronologie U-Pb sur zircon et contexte structural. Comptes Rendus de l'Académie des Sciences 314, 1355–1362.

Theunissen, K., Klerkx, J., Melnikov, A., and Mruma, A., 1996. Mechanisms of inheritance of rift faulting in the western branch of the east African Rift, Tanzania. Tectonics 15, 776–790.

1127 Van Straaten, V.P., 1984. Gold Mineralization in Tanzania – a review, in: Foster, R.P., (Eds.), Gold
1128 '82: the Geology, Geochemistry and Genesis of Gold Deposits. A.A. Balkema, Rotterdam,
1129 pp. 673–685.
1130
1131 Vervoort, J.D. and Blichert-Toft, J., 1999. Evolution of the depleted mantle: Hf isotope evidence from
1132 juvenile rocks through time. Geochimica et Cosmochimica Acta 63, 533–556.
1133
1134 Walter, M.J., 1998. Melting of garnet peridotite and the origin of komatiite and depleted lithosphere.
1135 Journal of Petrology 39, 29–60.
1136
1137 Wendt, I., Besang, C., Harre, W., Kreuzer, H., Lenz, H. and Muller, P. 1972. Age determinations of
1138 granitic intrusions and metamorphic events in the early Precambrian of Tanzania. Proceedings
1139 of 24th International Geological Congress, Montreal, Canada, pp 295–314 (section 1).
1140
1141 Whitehouse, M.J., and Kemp, A.I.S., 2010. On the difficulty of assigning crustal residence, magmatic
1142 protolith and metamorphic ages to Lewisian granulites: constraints from combined in situ U-
1143 Pb and Lu-Hf isotopes, in: Law, R.D., Butler, R.W.H., Holdsworth, R.E., Krabbendam, M.,
1144 and Strachan, R.A., (Eds.), Continental Tectonics and Mountain Building; the Legacy of
1145 Peach and Horne. Geological Society Special Publications 335, pp. 81–101.
1146
1147 Winchester, J.A., and Floyd, P.A., 1977. Geochemical discrimination of different magma series and
1148 their differentiation products using immobile elements. Chemical Geology 20, 325–343.
1149
1150 Wiedenbeck, M., Allé, P., Corfu, F., Griffin, W.L., Meier, M., Oberli, F., Von Quadt, A., Roddick,
1151 J.C., and Spiegel, W., 1995. Three natural zircon standards for the U-Th-Pb, Lu-Hf, trace
1152 element and REE analysis. Geostandards and Geoanalytical Research 19, 1–23.
1153

Wood, D.A., 1980. The application of a Th-Hf-Ta diagram to problems of tectonomagmatic classification and to establishing the nature of crustal contamination of basaltic lavas of the British Tertiary volcanic province. Earth and Planetary Sciences Letters 50, 11–30.

Zhoa, G., Cawood, P.A., Wilde, S.A., and Sun, M., 2002. Review of global 2.1–1.8 Ga orogens: implications for a pre-Rodinia supercontinent. Earth Science Reviews 59, 125–162.

Figure Captions

Figure 1

(a) Regional geology map of SW Tanzania showing Ubendian Terranes (modified from Daly, 1988); (b) existing tectonic model for Paleoproterozoic accretion of Ubendian Terranes (Daly, 1988).

Figure 2

Regional geologic map showing Ubendian Terranes and previously reported geochronology sample locations (modified from Smirnov et al., 1973).

Figure 3

Local geology map showing the location of geochronology and lithogeochemistry samples. Inferred lithologic contacts are based on a series of river traverses by the first author and are integrated with unpublished aeromagnetic and radiometric surveys, acquired from Helio Resource Corp. Shear zone locations are based, in part, on mapping and correspond to negative magnetic anomalies, whereas dikes are buried and interpreted from linear magnetic highs. Contour lines are based on an unpublished digital elevation model by Helio Resource Corp. and are shown at 5 m intervals.

Figure 4

(a) Folded banding in Archean granite in sharp contact with massive gabbroic dike; (b) well developed banding in foliated granite; (c) foliated Archean granitoid (CL098) cross cut by massive granodiorite dike (CL0911); (d) weathered surface of Ilunga Syenogranite that gives surface

1182 expposures a grey appearance. When fresh, modally dominant pink K feldspar crystals are visible.
1183 Narrow aplitic dike observed crosscutting the Ilunga Syenogranite; (e) Ilunga Syenogranite in drill
1184 core from Porcupine ore body; (f) gold- and pyrite-bearing quartz vein cross cutting Ilunga
1185 Syenogranite; (g) mafic enclave suggesting the Ilunga Syenogranite is pre-dated by mafic intrusions;
1186 (h) porphyritic monzogranite showing characteristic K feldspar phenocrysts; (i) Saza Granodiorite
1187 cross cut by aplite dike. The pitted weathered profile is typical of Saza Granodiorite outcrops; (j) Saza
1188 Granodiorite in drill core (CL1030).
1189
1190 Figure 5
1191 (a) Typical example of the diorite-gabbro suite in core; (b) finer grained example of diorite-gabbro
1192 suite with more felsic enclaves; (c) plagioclase-amphibole intergrowths in diorite; (d) core photo of an
1193 example of the undifferentiated diorite-gabbro-granodiorite unit (Fig. 3) showing variable grain-size
1194 and modal mineralogy at hand sample scale; (e) complex and poly-phase mafic enclave hosted by
1195 granodiorite. Note ductile flow evidence around the enclave; (f) late fine-grained and alkaline dike
1196 (CL0956) cross cutting foliated Archean granitoid.
1197
1198 Figure 6
1199 (a) Transmitted light photomicrograph of primary Fe-Mg minerals in foliated Archean granite that
1200 have been replaced by chlorite, titanite, epidote, and opaques; (b) transmitted light photomicrograph
1201 of rare relict amphibole in a granodiorite dike that has been overprinted by chlorite and epidote; (c)
1202 transmitted light photomicrograph of diorite dike showing characteristic mineral assemblage of
1203 amphibole, plagioclase, quartz, titanite, and epidote; (d) crossed nicols transmitted light
1204 photomicrograph of recrystallized quartz grain boundaries in foliated Archean granitoid. Quartz
1205 crystals also locally possess undulatory extinction and subgrain development; (e) crossed nicols
1206 transmitted light photomicrograph of sericitized plagioclase; (f) crossed nicols transmitted light
1207 photomicrograph of micrographic texture in Ilunga Syenogranite. Locally, Ilunga Syenogranite
1208 samples possess gradational contacts with aplite dikes and are characterized by abundant feldspar
1209 intergrowth textures.

1210

1211 Figure 7

1212 Concordia plots for CL0911, CL0972, and CL0975, respectively. See text for discussion.

1213

1214 Figure 8

1215 (a) Cathodoluminesence image of zircon F1 from CL109 showing ablation spots and concordant

1216 $^{207}Pb/^{206}Pb$ ages; (b) cathodoluminesence image of zircon H1 from CL1019 showing ablation spots

1217 and concordant $^{207}Pb/^{206}Pb$ ages; (c) cathodoluminesence image of zircon J8 from CL1020 showing

1218 U-Pb and Lu-HF ablation spots and concordant $^{207}Pb/^{206}Pb$ ages; (e) cathodoluminesence image of

1219 zircon B1 from CL1022 showing ablation spots and concordant $^{207}Pb/^{206}Pb$ ages.

1220

1221 Figure 9

1222 (a, b) Concordia plots of all Archean LA-MC-ICP-MS zircon analyses and concordant (>95%

1223 concordance) analyses, respectively. See text for discussion.

1224

1225 Figure 10

1226 (a, heb) Concordia plots of all Proterozoic LA-MC-ICP-MS zircon analyses and concordant (>95%

1227 concordance) analyses, respectively. See text for discussion.

1228

1229 Figure 11

1230 (a) Measured $^{176}Hf/^{177}Hf$ ratios from CL098, CL109, and CL1020. Overlying individual analyses are

1231 the probability distributions for each sample. Samples CL098 and CL1020 possess approximately

1232 normal $^{176}Hf/^{177}Hf$ ratios distributions, whereas CL109 possesses a weakly bi-modal distribution. (b)

1233 Calculated $^{176}Hf/^{177}Hf_{initial}$ ratios for sample CL098, CL109, and CL1020 plotted against each analyses

1234 corresponding $^{207}Pb/^{206}Pb$ age. The CHUR evolution line and typical 2σ uncertainty for an individual

1235 analysis are also shown. (c) Calculated εHf for samples CL098, CL109, and CL1020 plotted against

1236 the corresponding $^{207}Pb/^{206}Pb$ age for each analysis. DM (MORB source depleted mantle, Griffin et

1237 al., 2000), Slave Craton mantle (Pietranik et al., 2008), and Neo-Mesoarchean mantle (Shirey et al.,

2008) are also plotted. The typical 2σ uncertainty on individual $^{207}Pb/^{206}Pb$ ages and εHf values are also shown.

Figure 12

Trace element rock classification diagram (modified from Pearce, 1996a). See text for discussion.

Figure 13

(a) REE plot of felsic phases normalized to CL chondrite (Sun and McDonough, 1989); (b) trace element plot of felsic phases normalized to primitive mantle (Sun and McDonough, 1989); (c) REE plot of intermediate-mafic phases normalized to CL chondrite (Sun and McDonough, 1989); (d) trace element plot of intermediate-mafic phases normalized to primitive mantle (Sun and McDonough, 1989); (e) REE plot of foliated Archean granitoids plotted with Tanzania Craton REE sample range from Manya (2011). REE are normalized to CI chondrite (Sun and McDonough, 1989). (f) trace element plot of foliated Archean granitoids plotted with Tanzania Craton REE sample range from Manya (2011). Trace elements are normalized to primitive mantle (Sun and McDonough, 1989). Sample symbols are the same as Fig. 12.

Figure 14

(a) La vs. La/Sm plot of diorite-gabbro suite. (b) Sm vs. Sm/Yb plot of diorite gabbro suite. Melting curves are from the non-modal batch melting equations of Shaw (1970). The modelling used spinel lherzolite (with mode = $olivine_{53} + orthopyroxene_{27} + clinopyroxene_{17} + spinel_3$; melt mode = $olivine_6 + orthopyroxene_{28} + clinopyroxene_{67} + spinel_{11}$; Kinzler, 1997) and garnet lherzolite (with mode = $olivine_{60} + orthopyroxene_{20} + clinopyroxene_{10} + garnet_{10}$; melt mode = $olivine_3 + orthopyroxene_{16} + clinopyroxene_{88} + garnet_9$; Walter, 1998) sources with depleted mantle (DMM; McKenzie and O'Nions, 1991) and primitive mantle (PM; Sun and McDonough, 1989) compositions. Mineral/matrix partition coefficients are from McKenzie and O'Nions (1991). N-MORB and E-MORB compositions were taken from Sun and McDonough (1989). The solid line represents the mantle array and is defined using the DMM and PM compositions. Lithology sample symbols are the same as Fig. 12.

Figure 15

(a) Basaltoid tectonic discrimination diagram modified from Shervais (1982). VAB = volcanic arc basalt, MORB = mid-ocean ridge basalt, BAB = back-arc basin basalt, OIB = ocean island basalt, CAB = continental arc basalt; (b) basaltoid tectonic discrimination diagram modified from Wood (1980). N-MORB = normal-mid ocean ridge basalt; (c) basaltoid tectonic discrimination diagram modified from Meschede (1986). WPT = within-plate tholeitic basalt, WPA = within-plate alkalic basalt, P-type MORB = primitive mid-ocean ridge basalt, N-type MORB = normal-type mid-ocean ridge basalt; (d) basaltoid tectonic discrimination diagram modified from Pearce (1983). S = subduction zone enrichment trend, C = crustal contamination trend, F = fractional crystallization trend (F = 0.5); (e) log-transformed basaltoid discrimination diagram modified from Agrawal et al. (2008). DF1=0.3518 Log(La/Th)+0.6013 Log(Sm/Th)−1.3450 Log(Yb/Th)+2.1056 Log(Nb/Th)−5.4763; and DF2 = −0.3050 Log(La/Th) − 1.1801 Log(Sm/Th) + 1.6189 Log(Yb/Th) + 1.2260 Log(Nb/Th) − 0.9944. MORB = mid-ocean ridge basalts, IAB = island arc basalt, CRB = continental rift basalt, OIB = ocean island basalt; (f) log-transformed basaltoid discrimination diagrams modified from Agrawal et al. (2008). DF1 = 0.5533 Log(La/Th) + 0.2173 Log(Sm/Th) − 0.0969 Log(Yb/Th) + 2.0454 Log(Nb/Th) − 5.6305 and DF2 = −2.4498 Log(La/Th) + 4.8562 Log(Sm/Th) − 2.1240 Log(Yb/Th) − 0.1567 Log(Nb/Th) + 0.94. IAB = island arc basalt, OIB = ocean island basalt, CRB = continental rift basalt. Lithology symbols are the same as Fig. 12.

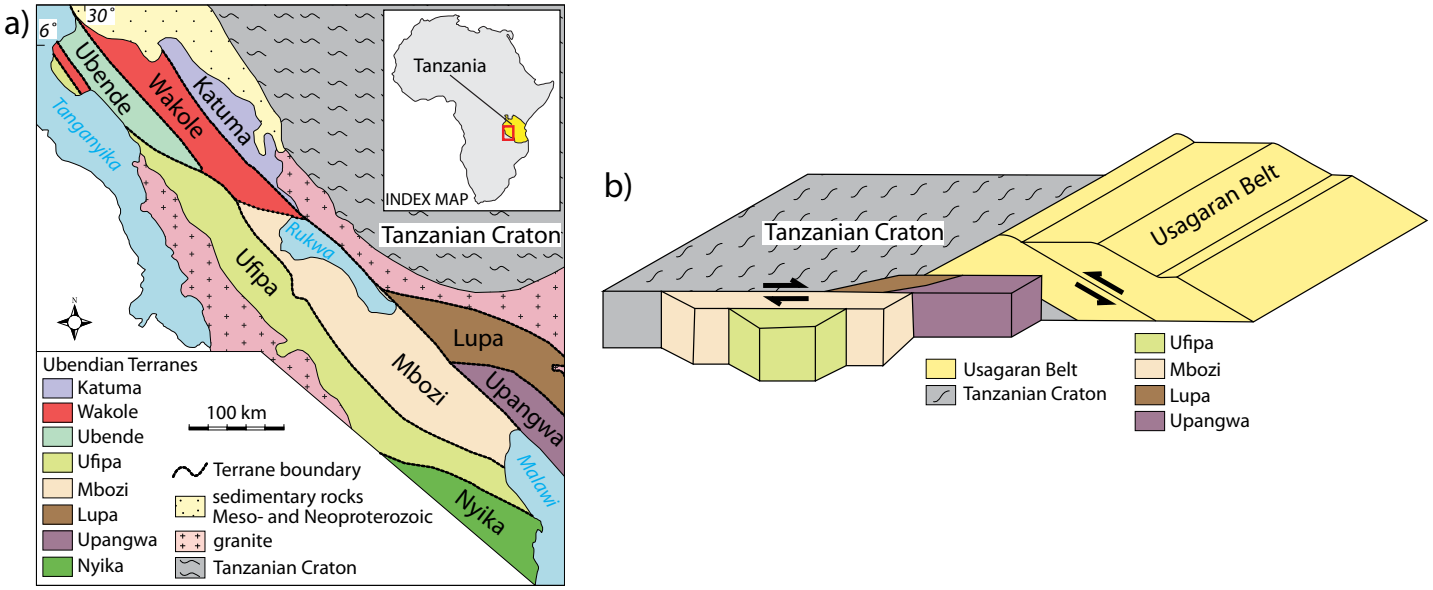
a)
6°
30°
Ubende
Wakole
Katuma
Tanganyika
Rukwa
Ufipa
Mbozi
Lupa
Upangwa
Nyika
Malawi
Tanzania
INDEX MAP
Tanzanian Craton
Ubendian Terranes
Katuma
Wakole
Ubende
Ufipa
Mbozi
Lupa
Upangwa
Nyika
100 km
Terrane boundary
sedimentary rocks
Meso- and Neoproterozoic
granite
Tanzanian Craton
b)
Tanzanian Craton
Usagaran Belt
Usagaran Belt
Tanzanian Craton
Ufipa
Mbozi
Lupa
Upangwa

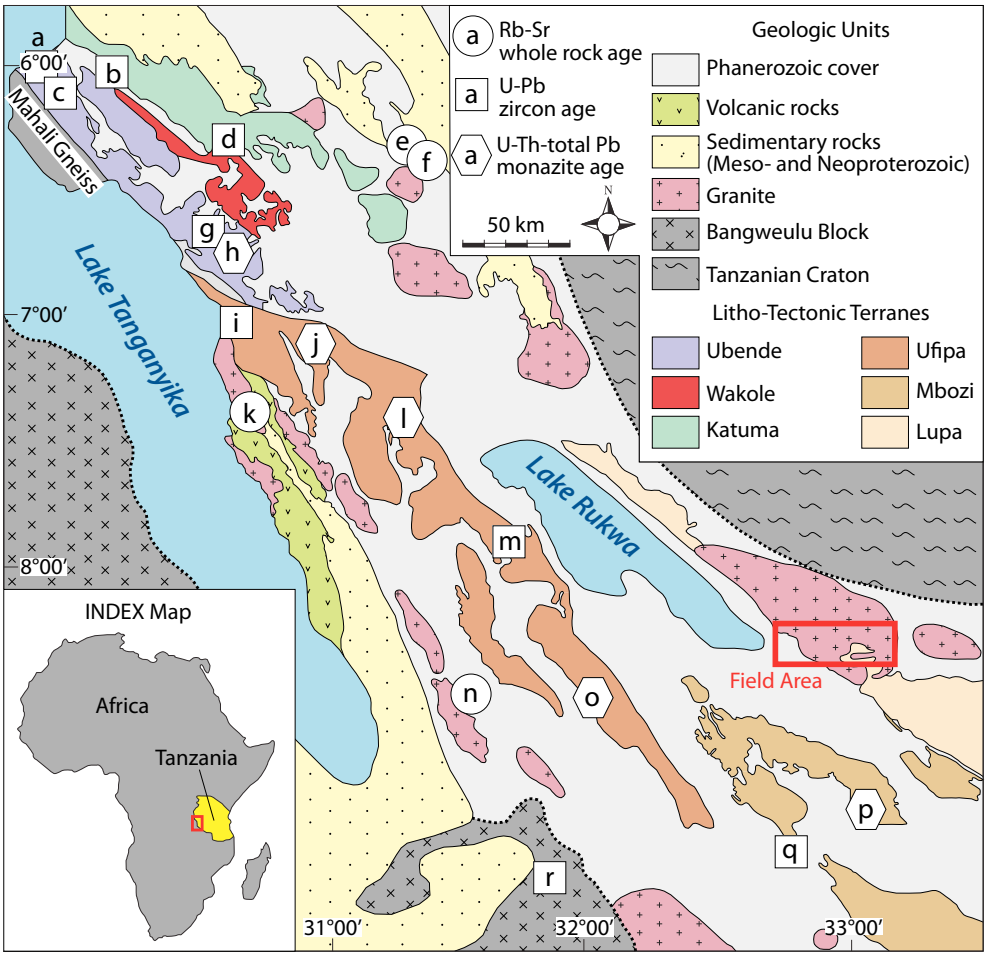

a 1854 ± 26 Ma (eclogite)[1]

b 1977 ± 40 Ma (mafic granulite)[1]

c 1817 ± 26 Ma (metapelite)[1]
1093 ± 10 Ma (metapelite)[1]

d 1900 ± 14 Ma (metapelite)[1]

e 1847 ± 37 Ma (granite)[2]

f 1902 ± 73 Ma (gneiss)[2]

g 1866 ± 14 Ma (eclogite)[1]

h 1831 ± 11 Ma (metapelite)[1]
1175 ± 10 Ma (metapelite)[1]
601 ± 7 Ma (metapelite)[1]

i 1864 ± 32 Ma (granite)[2]

j 1868 ± 55 Ma (metapelite)[1]
578 ± 63 Ma (metapelite)[1]

k 1725 ± 48 Ma (granite)[2]

l 566 ± 8 Ma (metapelite)[1]

m 1901 ± 37 Ma (metapelite)[1]

n 1723 ± 41 Ma (granite)[2]

o 1919 ± 12 Ma (metapelite)[1]

p 1814 ± 7 Ma (metapelite)[1]

q 743 ± 30 Ma (syenite)[3]

r 1838 ± 86 Ma (granite)[4]

s 1930 ± 30 Ma (Nyika granite; off map)[5]

[1]Boniface (2009); [2]Lenoir et al. (1994); [3]Brock (1963); [4]Schandelmeirer (1983); [5]Dodson et al. (1975)

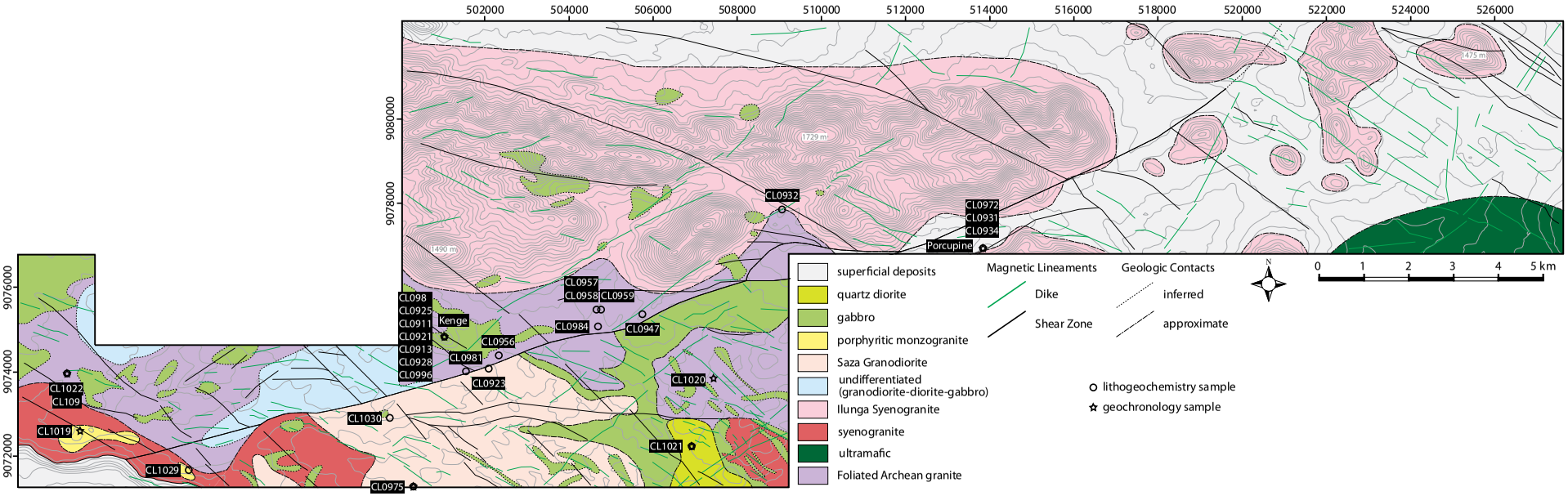
502000
504000
506000
508000
510000
512000
514000
516000
518000
520000
522000
524000
526000
9080000
9078000
9076000
9074000
9072000
1729 m
1490 m
1475 m
CL0932
CL0972
CL0931
CL0934
Porcupine
CL0957
CL0958
CL0959
CL098
CL0925
CL0911
CL0921
CL0913
CL0928
CL0996
Kenge
CL0984
CL0947
CL0956
CL0981
CL0923
CL1020
CL1022
CL109
CL1019
CL1030
CL1021
CL1029
CL0975
superficial deposits
quartz diorite
gabbro
porphyritic monzogranite
Saza Granodiorite
undifferentiated (granodiorite-diorite-gabbro)
Ilunga Syenogranite
syenogranite
ultramafic
Foliated Archean granite
Magnetic Lineaments
Dike
Shear Zone
Geologic Contacts
inferred
approximate
lithogeochemistry sample
geochronology sample
N
0
1
2
3
4
5 km

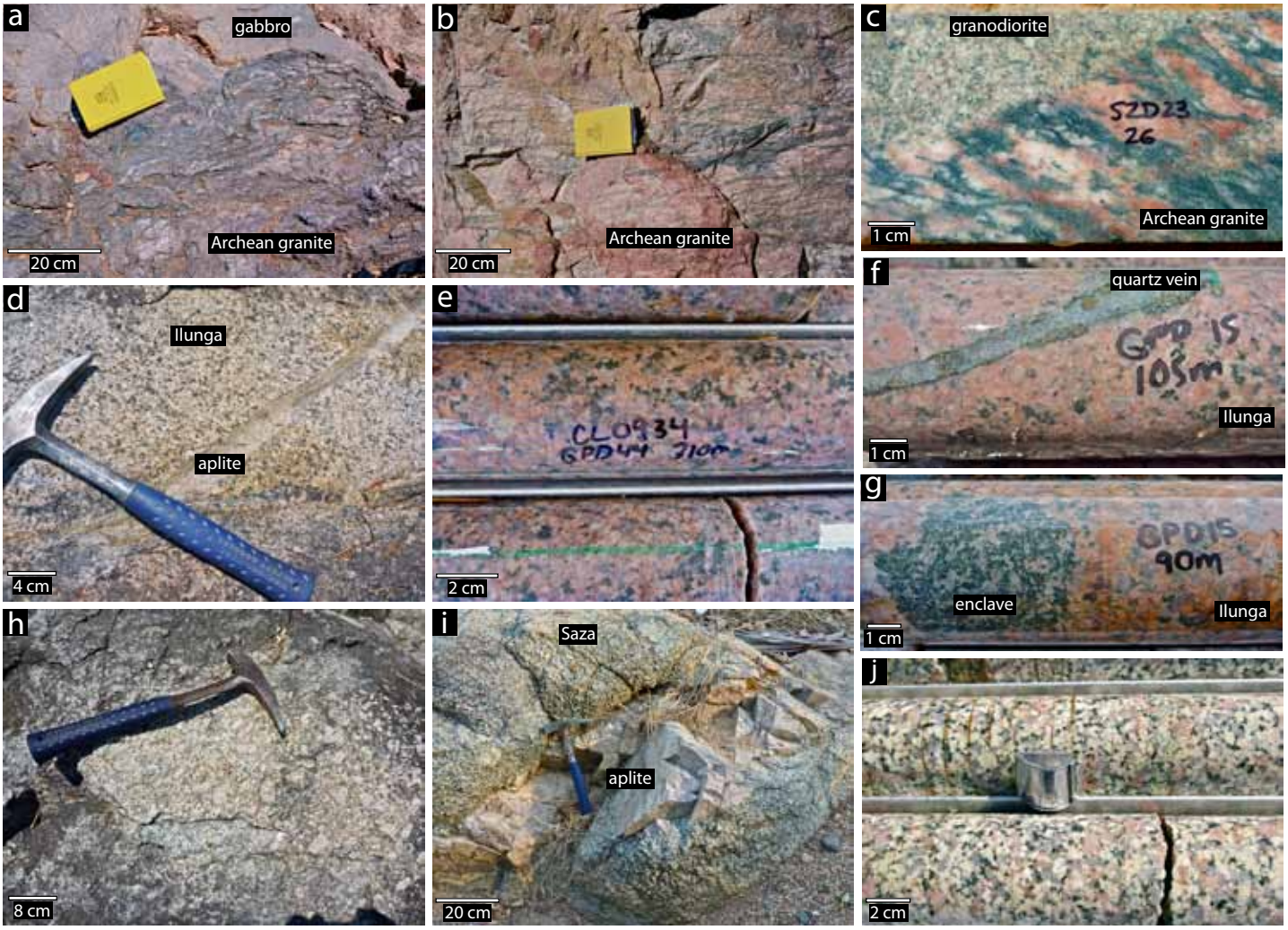
a
gabbro
Archean granite
20 cm
b
Archean granite
20 cm
c
granodiorite
SZD23
26
Archean granite
1 cm
d
Ilunga
aplite
4 cm
e
CL0934
GPD44
2 cm
f
quartz vein
Ilunga
1 cm
g
GPD15
90m
enclave
Ilunga
1 cm
h
8 cm
i
Saza
aplite
20 cm
j
2 cm

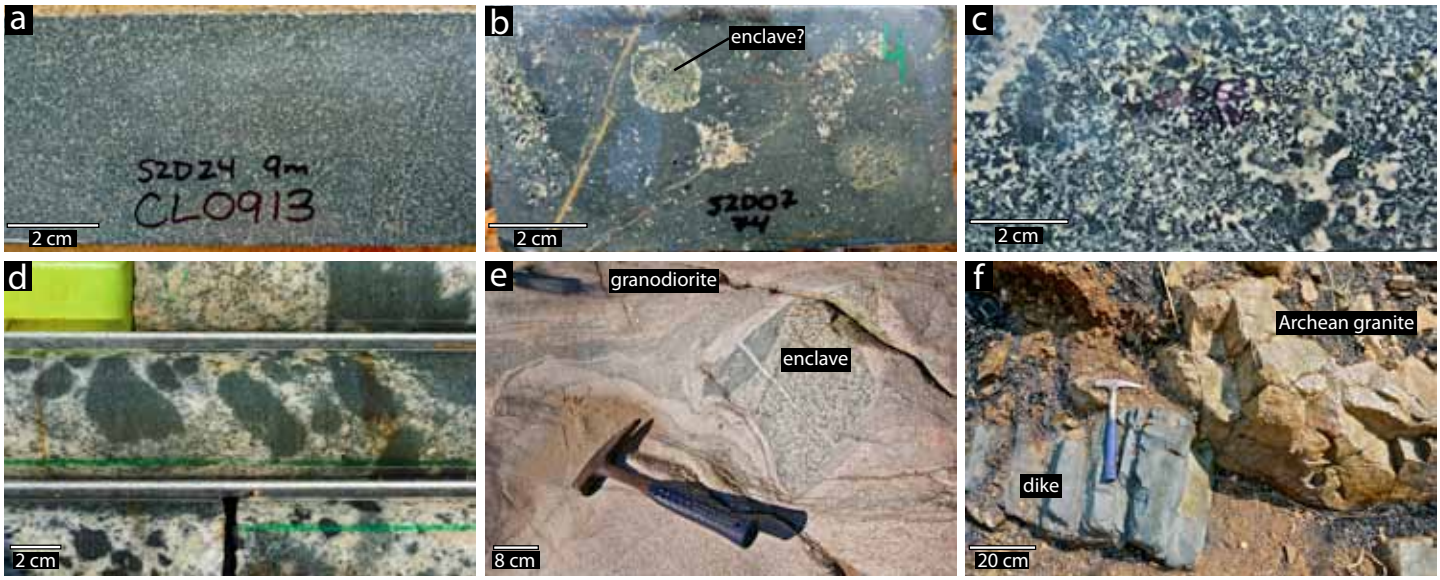
a
52D24 9m
CL0913
2 cm
b
enclave?
52D07
2 cm
c
2 cm
d
2 cm
e
granodiorite
enclave
8 cm
f
Archean granite
dike
20 cm

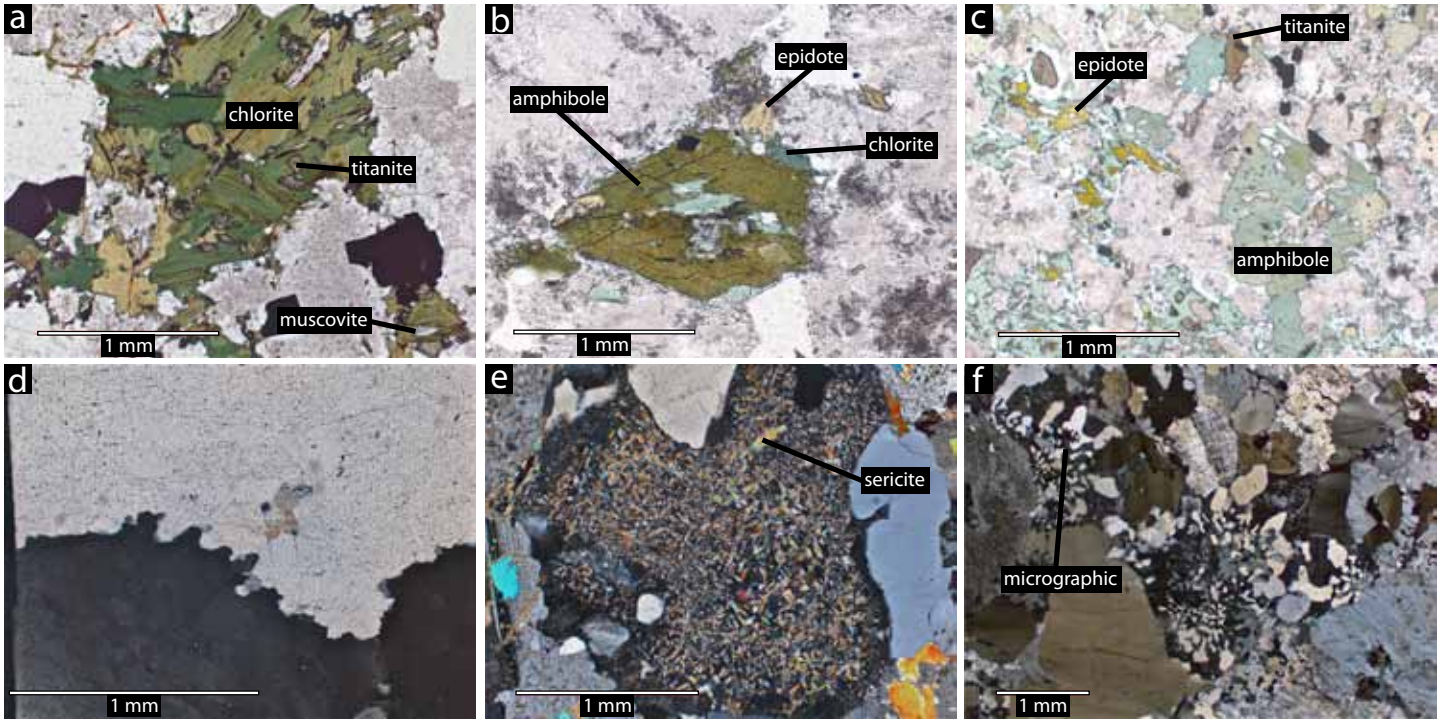
a
chlorite
titanite
muscovite
1 mm
b
epidote
amphibole
chlorite
1 mm
c
titanite
epidote
amphibole
1 mm
d
1 mm
e
sericite
1 mm
f
micrographic
1 mm

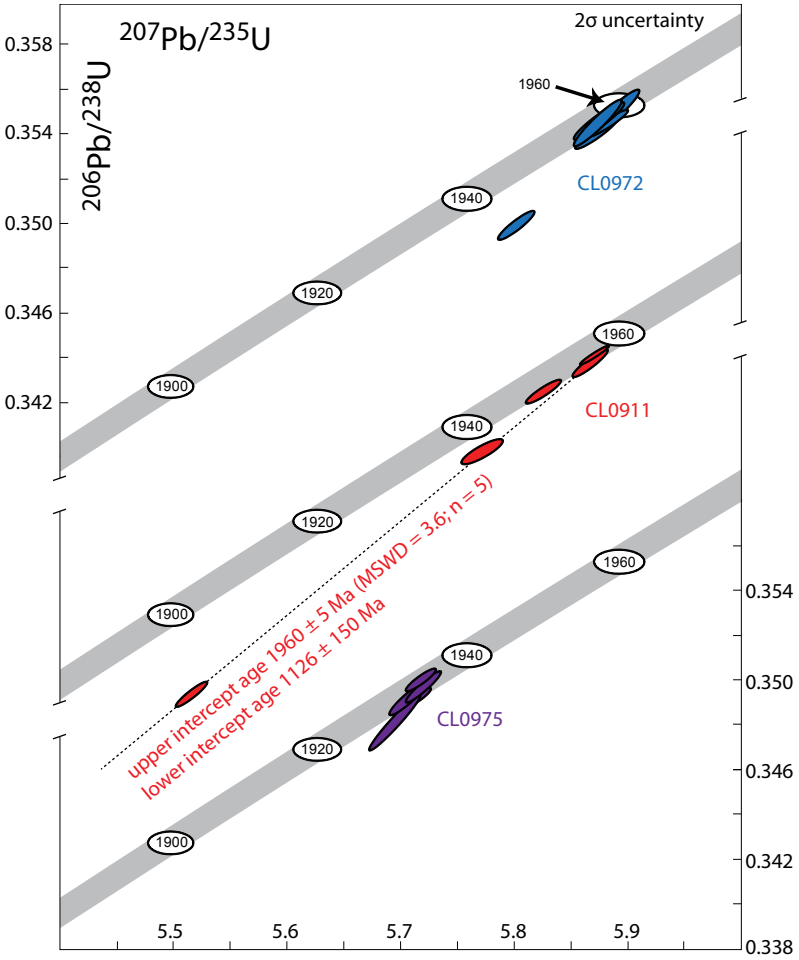
$^{207}Pb/^{235}U$
$^{206}Pb/^{238}U$
2σ uncertainty
0.358
0.354
0.350
0.346
0.342
0.338
5.5
5.6
5.7
5.8
5.9
1960
1940
1920
1900
CL0972
CL0911
CL0975
upper intercept age 1960 ± 5 Ma (MSWD = 3.6; n = 5)
lower intercept age 1126 ± 150 Ma

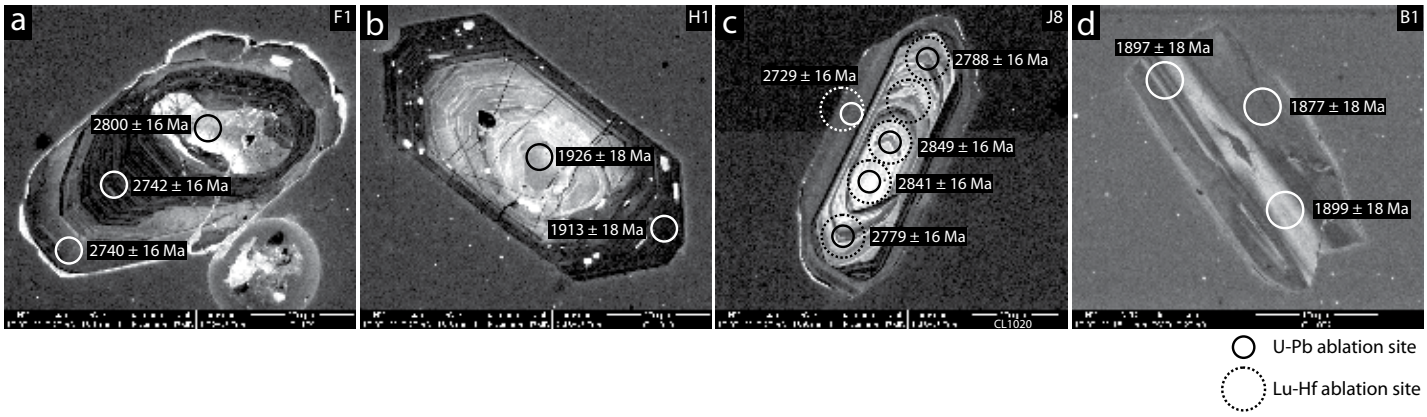
a
F1
2800 ± 16 Ma
2742 ± 16 Ma
2740 ± 16 Ma
b
H1
1926 ± 18 Ma
1913 ± 18 Ma
c
J8
2729 ± 16 Ma
2788 ± 16 Ma
2849 ± 16 Ma
2841 ± 16 Ma
2779 ± 16 Ma
CL1020
d
B1
1897 ± 18 Ma
1877 ± 18 Ma
1899 ± 18 Ma
U-Pb ablation site
Lu-Hf ablation site

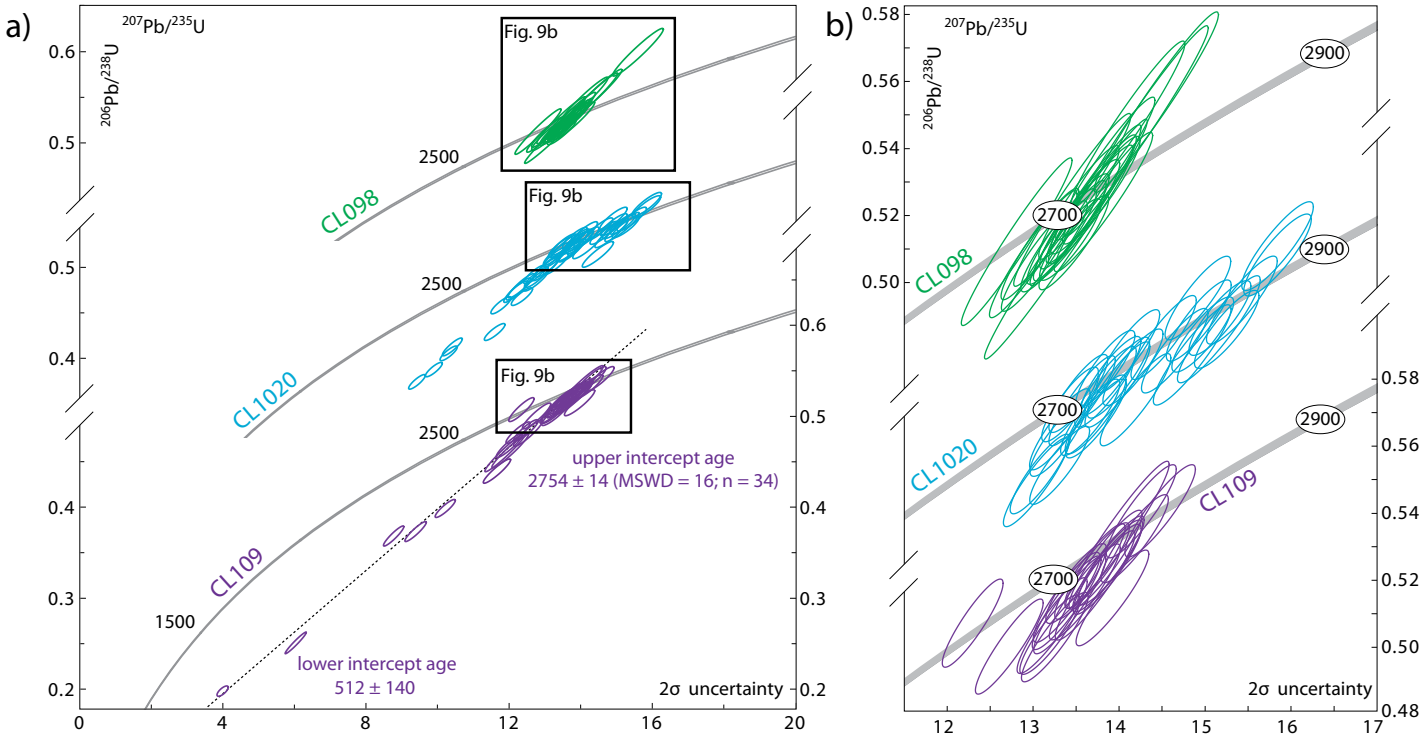
a)
$^{207}Pb/^{235}U$
$^{206}Pb/^{238}U$
Fig. 9b
Fig. 9b
Fig. 9b
2500
2500
2500
1500
CL098
CL1020
CL109
upper intercept age
2754 ± 14 (MSWD = 16; n = 34)
lower intercept age
512 ± 140
2σ uncertainty
b)
$^{207}Pb/^{235}U$
$^{206}Pb/^{238}U$
2900
2900
2900
2700
2700
2700
CL098
CL1020
CL109
2σ uncertainty

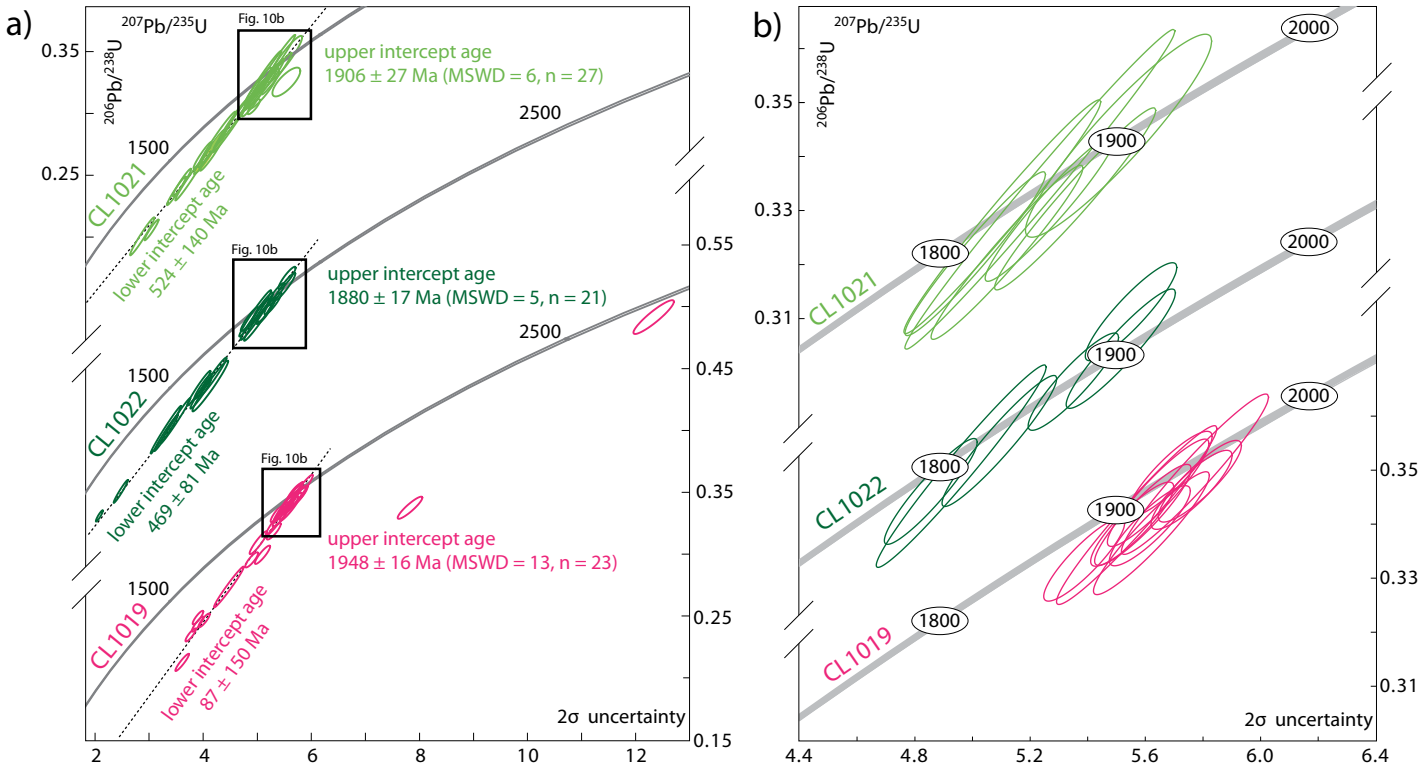
a)
b)
$^{207}Pb/^{235}U$
$^{206}Pb/^{238}U$
Fig. 10b
upper intercept age
1906 ± 27 Ma (MSWD = 6, n = 27)
lower intercept age
524 ± 140 Ma
CL1021
upper intercept age
1880 ± 17 Ma (MSWD = 5, n = 21)
lower intercept age
469 ± 81 Ma
CL1022
upper intercept age
1948 ± 16 Ma (MSWD = 13, n = 23)
lower intercept age
87 ± 150 Ma
CL1019
2σ uncertainty
1500
2500
1800
1900
2000

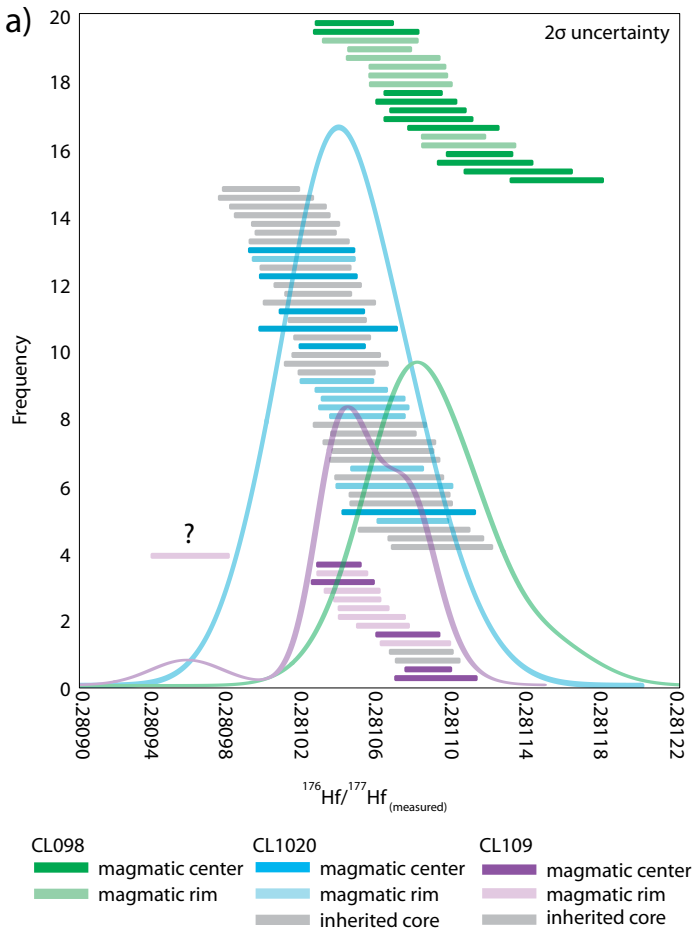
a)
2σ uncertainty
Frequency
?
$^{176}Hf/^{177}Hf_{(measured)}$
CL098
magmatic center
magmatic rim
CL1020
magmatic center
magmatic rim
inherited core
CL109
magmatic center
magmatic rim
inherited core

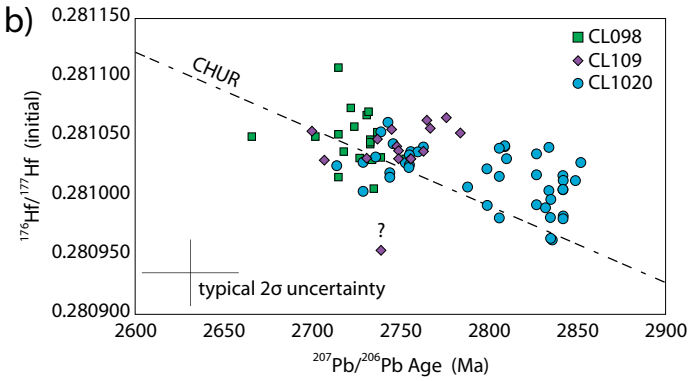
b)
CHUR
CL098
CL109
CL1020
?
typical 2σ uncertainty
$^{176}Hf/^{177}Hf$ (initial)
$^{207}Pb/^{206}Pb$ Age (Ma)

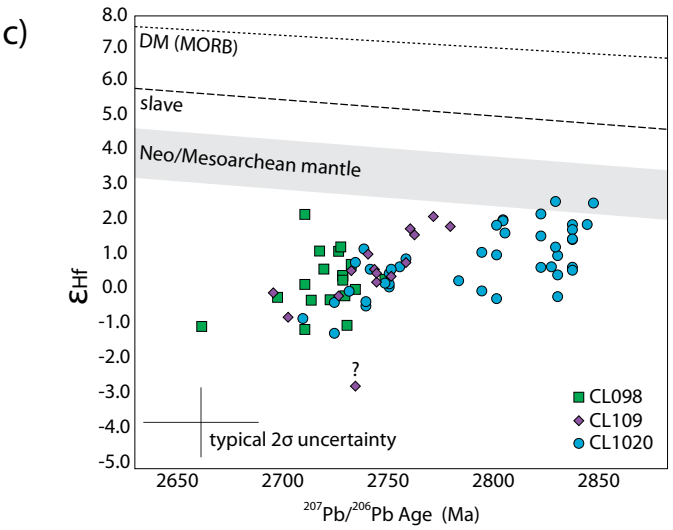
c)
DM (MORB)
slave
Neo/Mesoarchean mantle
εHf
?
typical 2σ uncertainty
CL098
CL109
CL1020
$^{207}Pb/^{206}Pb$ Age (Ma)

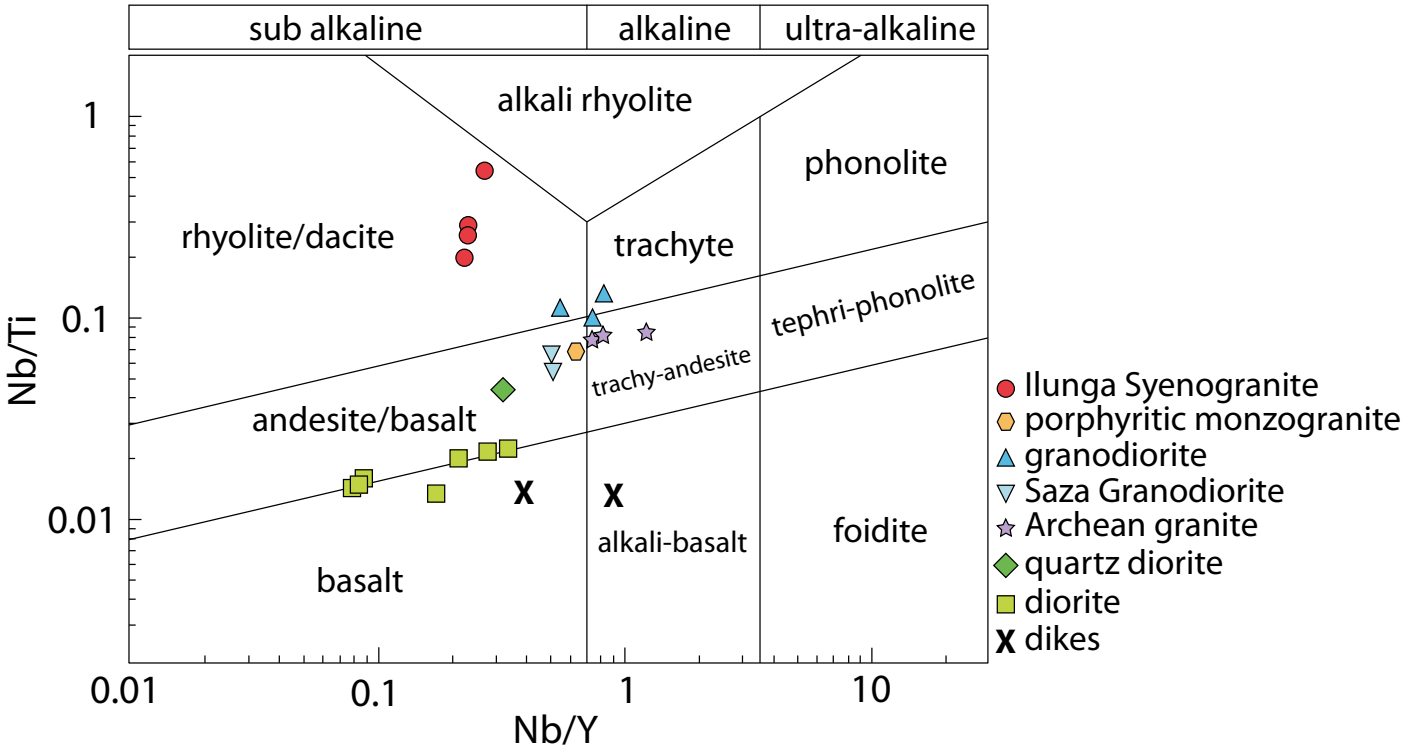
sub alkaline
alkaline
ultra-alkaline
alkali rhyolite
phonolite
rhyolite/dacite
trachyte
tephri-phonolite
trachy-andesite
andesite/basalt
alkali-basalt
foidite
basalt
Nb/Ti
Nb/Y
1
0.1
0.01
0.01
0.1
1
10
Ilunga Syenogranite
porphyritic monzogranite
granodiorite
Saza Granodiorite
Archean granite
quartz diorite
diorite
dikes

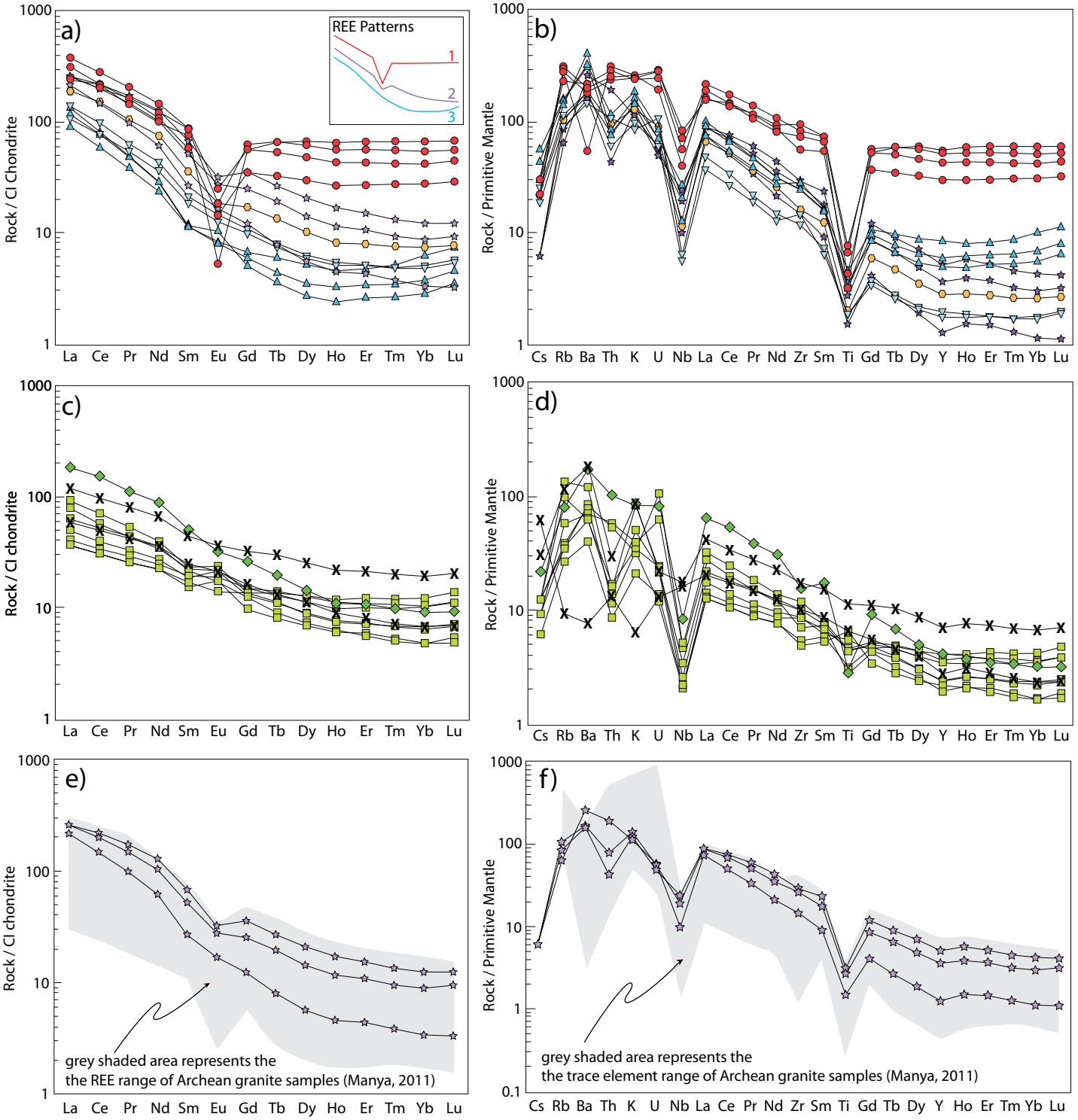
a)
REE Patterns
1
2
3
Rock / CI Chondrite
1000
100
10
1
La Ce Pr Nd Sm Eu Gd Tb Dy Ho Er Tm Yb Lu
b)
Rock / Primitive Mantle
Cs Rb Ba Th K U Nb La Ce Pr Nd Zr Sm Ti Gd Tb Dy Y Ho Er Tm Yb Lu
c)
Rock / CI chondrite
d)
Rock / Primitive Mantle
e)
Rock / CI chondrite
grey shaded area represents the
the REE range of Archean granite samples (Manya, 2011)
f)
Rock / Primitive Mantle
0.1
grey shaded area represents the
the trace element range of Archean granite samples (Manya, 2011)

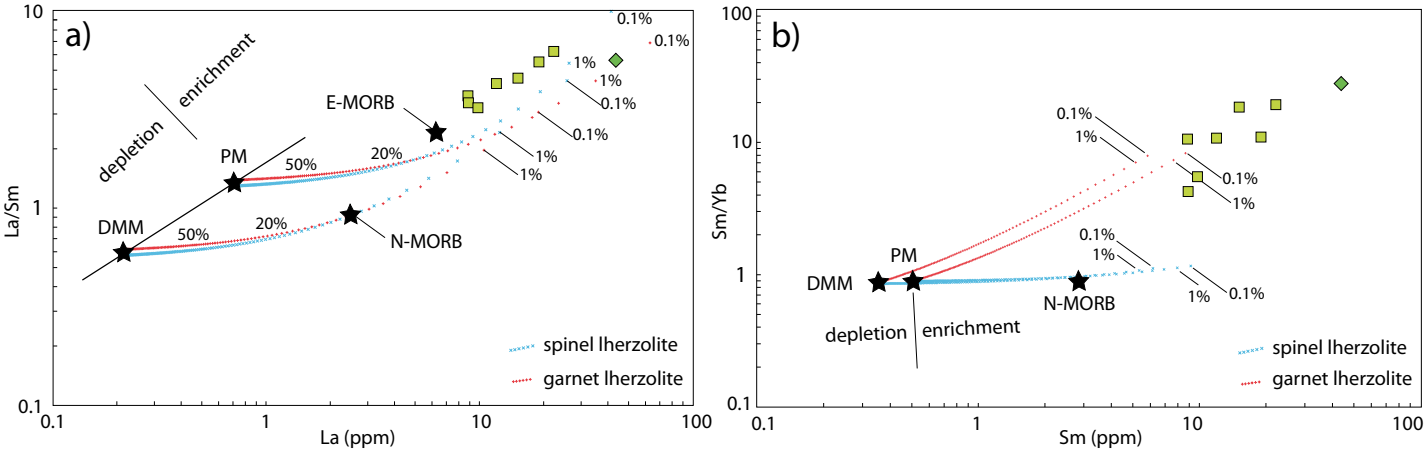
a)
enrichment
depletion
E-MORB
PM
DMM
N-MORB
50%
20%
50%
20%
0.1%
1%
spinel lherzolite
garnet lherzolite
La/Sm
La (ppm)
b)
PM
DMM
N-MORB
depletion
enrichment
Sm/Yb
Sm (ppm)

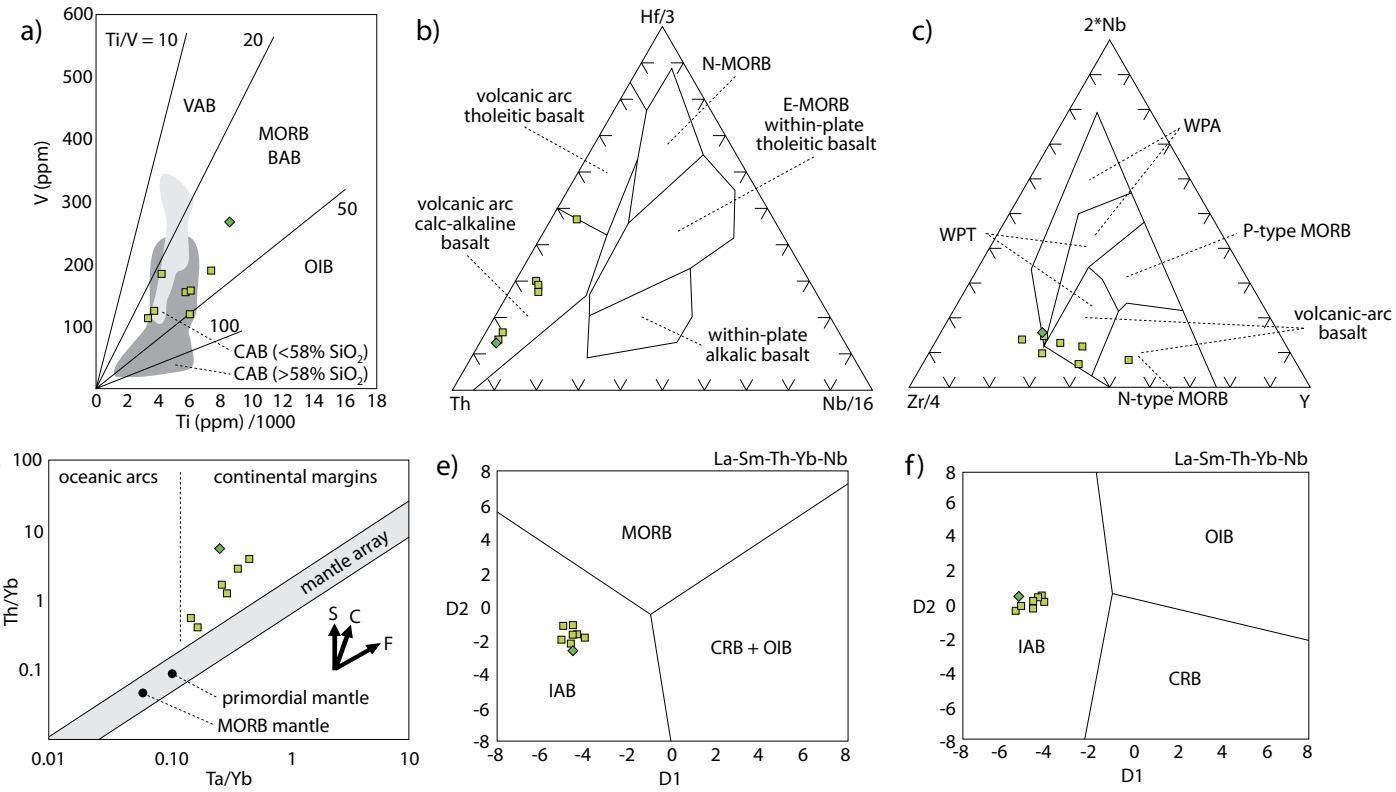
a)
Ti/V = 10
20
50
100
VAB
MORB
BAB
OIB
CAB (<58% SiO2)
CAB (>58% SiO2)
V (ppm)
Ti (ppm) /1000
b)
Hf/3
N-MORB
E-MORB
within-plate
tholeitic basalt
volcanic arc
tholeitic basalt
volcanic arc
calc-alkaline
basalt
within-plate
alkalic basalt
Th
Nb/16
c)
2*Nb
WPA
WPT
P-type MORB
volcanic-arc
basalt
N-type MORB
Zr/4
Y
d)
oceanic arcs
continental margins
mantle array
S
C
F
primordial mantle
MORB mantle
Th/Yb
Ta/Yb
e)
La-Sm-Th-Yb-Nb
MORB
CRB + OIB
IAB
D2
D1
f)
La-Sm-Th-Yb-Nb
OIB
IAB
CRB
D2
D1